UNIVERSITÀ DEGLI STUDI DI PADOVA

Dipartimento di Fisica e Astronomia "Galileo Galilei"

Master Degree in Physics

Final Dissertation

Morphology of cosmic reionisation from intensity mapping

Thesis supervisor

Prof. Sabino Matarrese

Thesis co-supervisor

Dr. Carlo Schimd

Candidate

Benedetta Spina

Academic Year 2018/2019

Acknowledgments

I would first like to thank Prof. Sabino Matarrese for the invaluable help and time he dedicated to me during this thesis and the all master, without which this work would have never been possible.

I owe a very special thank to Dr. Carlo Schimd, who encouraged and supported me during the Erasmus period in Marseille and the thesis work. If I am so much passionate and even amused by cosmology, the credit is mostly yours. Not to mentioned you taught me how to make pastry cream.

Furthermore I would like to thank Prof. Matteo Viel and Dr. Marta Spinelli for providing the material and simulations on which the thesis is based as well for the support and the help on the way.

I would also like to thank my parents, my brothers and my family for believing in me since I was eight and I was dreaming of becoming a scientist (whatever it means) as a grown-up. And thanks Simone, how did you manage to stand by me even in the most difficult moments is still a mystery to me.

Contents

Introduction

The aim of this thesis is to explore the very complex spatial structure of the reionization field in standard and alternative cosmologies, with cold or warm dark matter and cosmological constant. Existing and upcoming radio-telescopes like LOFAR (van Haarlem et al., 2013), CONCERTO (Kovetz et al., 2017) and SKA-1 (Square Kilometre Array Cosmology Science Working Group et al., 2018) are designed to explore the dynamics of the reionization process and the role of ionization sources using the intensity mapping technique of the 21 cm (Bull et al., 2015) or other emission lines such as [CII] (Gong et al., 2012). Contrary to galaxy redshift surveys, intensity mapping can survey efficiently very large cosmological volumes and eventually be used to address questions of fundamental cosmology: is there any signature of primordial non-Gaussianities (Wyithe and Morales, 2007) in intensity mapping? Is reionization affected by the nature of dark matter and possibly prove evidence for warm dark matter (Carucci et al., 2015)? This thesis focuses on the last question and analyzes three different cosmologies with cold dark matter as reference or warm dark matter (with particles' masses of $m_{\mathrm{WDM}} = 2,\ 3\,\mathrm{keV}/c^2$), using Monte Carlo methods to simulate the distribution of neutral hydrogen (HI) based on dark-matter-only N-body simulations of the large scale structure. The statistical tools used to quantify such difference are the Minkowski Functionals (MFs), described in Mecke, Buchert, and Wagner (1994), spatial statistics offering a complete characterization of the morphology of any continuous random field (here the 21 cm temperature fluctuations, i.e. the intensity map) going beyond the two-points correlation functions: for a given thresholded field i.e. isocontour level of the intensity map, MFs measure the area, the perimeter and the Euler characteristic of the connected regions, which accounts of the number of isolated regions minus the number of holes. These statistics allow us to describe the spatial distribution of neutral hydrogen in a more complete way with respect to the commonly used halo mass function or the power spectrum. Improvements on the intensity mapping technique and the study of the HI amount in the Universe are fields of great interest nowadays and several efforts have been made to improve the accuracy of the results.

The first chapter reviews fundamentals of dark matter particles' physics (Peter and Uzan, 2009) and structure formation and the main physical processes during the reionization epoch (Barkana and Loeb, 2001). It is indeed the deep comprehension of the physics involved what can suggest the appropriate observables to study this epoch. The spin-flip transition between two states of the hydrogen atom (Field, 1958) is the most promising observable: the photons emitted have a specific wavelength of 21 cm and the intensity of such radiation is strong enough to be detected by the current instruments.

In Chapter 2, it is described the starting point of the thesis work. Starting from N-body simulations (Carucci et al., 2015) with cold or warm dark matter, for each catalogue the halo mass function, the power spectrum and the HI bias are computed. The second part accounts for the Monte Carlo simulation of the HI field, based on the previous N-body simulations and independent hydro-dynamical simulations, establishing a relation between the evolution of dark matter and neutral hydrogen haloes. Special care is devoted to the determination of the HI halo mass (Spinelli et al., 2019).

The projection of the three-dimensional HI field on the celestial sphere and the realization of 21 cm intensity maps tailored on the SKA1-MID and SKA1-LOW radio surveys are discussed in Chapter 3. The limits and the advantages of the intensity mapping technique are deeply analyzed and possible improvements are evaluated.

Finally, Chapter 4 is dedicated to the analysis of the intensity maps by Minkowski functionals. A comparative analysis as function of redshift, scale and dark matter mass is proposed.

Chapter 1

Reionization epoch and 21 cm cosmology

1.1 The pre-recombination Universe: dark matter candidates

Dark Matter (DM) is produced in the early universe and according to its velocity at decoupling from the thermal bath, one can distinguish between *cold*, *hot* and *warm* candidates, corresponding to high mass ($\sim$GeV or $>$TeV), intermediate mass ($\sim$keV) and small mass ($\sim$eV). The aim of this section it to review the constraints on the mass with respect to relic density observable today.

Suppose a gas of massive particles χ in thermodynamic equilibrium with their antiparticles $\bar{\chi}$ for $T \gg m_\chi$. If the dark matter interacts only gravitationally, then their interactions cannot guarantee thermal equilibrium and its density can be modified only by annihilation or inverse annihilation

$$\chi + \bar{\chi} \longleftrightarrow l + \bar{l}, \tag{1.1}$$

where l is a Standard Model particle. The reaction rate is $\Gamma_{\rm ann} = n_\chi \langle \sigma v \rangle$, where $\langle \sigma v \rangle$ is the cross section times the relative velocity thermally averaged over all possible initial states. A rule-of-thumb to define the equilibrium is by comparing $\Gamma_{\rm ann}$ with the expansion rate H. If $\Gamma_{\rm ann} \ll H$, then the equilibrium is never reach because DM particles do not interact in an Hubble time. If $\Gamma_{\rm ann} \gg H$ then the DM particles are in thermal equilibrium and the evolution of their abundance can be easily studied.

The density distribution at equilibrium (Peter and Uzan, 2009) reads

$$n_\chi = g_\chi \int \frac{\mathrm{d}^3 p}{(2\pi)^3} f_\chi(|\mathbf{p}|) \tag{1.2}$$

where the equilibrium distribution is

$$f_\chi^{\rm eq} = \frac{1}{\exp[(E_\chi - \mu_\chi)/T_\chi] \pm 1} \tag{1.3}$$

depending on the spin ("+" for Fermi-Dirac particles, "−" for Bose-Einstein particles). When the DM particles χ were in equilibrium, then their number density can be approximated by

$$n_\chi^{eq} = \begin{cases} g_{\text{eff}} \frac{\zeta(3)}{\pi^2} T^3 & T \gg m_\chi \\ g_\chi \left(\frac{m_\chi T}{2\pi}\right)^{3/2} e^{-\frac{m_\chi}{T}} & T \ll m_\chi \end{cases} \tag{1.4}$$

where the internal degrees of freedom are $g_{\text{eff}} = g_\chi$ for bosons and $\frac{3}{4} g_\chi$ for fermions (the general expression is achieved supposing a FD or BE distribution), also $\zeta(3) \simeq 1.2$.

1.1.1 Cold relics

For cold relics, decoupled from plasma when non-relativistic one has to solve the general Boltzmann equation

$$\mathcal{L}[f] = \mathcal{C}[f] \tag{1.5}$$

which describes the time evolution of a particle distribution f by the Liouville operator $\mathcal{L}$ and the collision operator $\mathcal{C}$. For a single DM component χ in a FRW cosmology the momentum-averaged equation yields the time evolution of the number density n_χ as

$$\dot{n}_\chi + 3Hn_\chi = -\langle \sigma v \rangle \left(n_\chi^2 - n_{\chi,eq}^2\right), \tag{1.6}$$

where $n_{\chi,eq}$ is the density distribution at equilibrium. The conservation of entropy allow us to write the number density as equation (1.6) and therefore becomes $\dot{n}_\chi + 3Hn_\chi = s\dot{Y}_\chi$, where $Y_\chi = n_\chi / s$ and s is the entropy density

$$s = \frac{2\pi^2}{45} g_{*s}(T) T^3, \tag{1.7}$$

which today is $s(t_0) = 2891.2\,\text{cm}^{-3}$. One therefore obtains

$$\dot{Y}_\chi = -\langle \sigma v \rangle s \left[Y_\chi^2 - Y_{\chi,eq}^2\right]. \tag{1.8}$$

Introducing the dimensionless variable

$$x_{FO} = \frac{m_\chi}{T_{FO}}, \tag{1.9}$$

the result for the freeze-out temperature is $x_{FO} \simeq 25$. Equation (1.8) becomes

$$\frac{\mathrm{d}Y_\chi}{\mathrm{d}x} = -\langle \sigma v \rangle \frac{s}{H\,x} \left[Y_\chi^2 - Y_{\chi,eq}^2\right] = -\frac{\Gamma_{\text{ann}}^{\text{eff}}}{H}. \tag{1.10}$$

It is useful to introduce the quantity $\Delta \equiv Y_\chi - Y_{\chi,eq}$, quation (1.10) therefore can be written as

$$\frac{\mathrm{d}\Delta}{\mathrm{d}x} = -\frac{\mathrm{d}Y_{\chi,eq}}{\mathrm{d}x} - \lambda x^{-2} \Delta \left(\Delta + 2Y_{\chi,eq}\right), \tag{1.11}$$

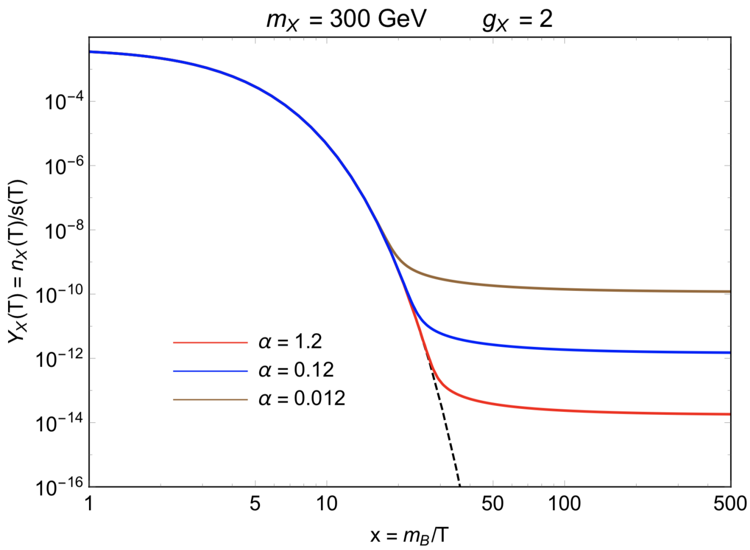

Figure 1.1: Standard freeze-out for three different cross sections.

with the dimensionless parameter

$$\lambda = \langle \sigma v \rangle \sqrt{\frac{\pi}{45}} \frac{g_*}{g_{s,*}^{1/2}} m_\chi M_P \tag{1.12}$$

encoding the fundamental parameters of χ.

For cold dark matter the Boltzmann equation can be solved approximately, in two regimes and then matching those solutions at the freeze-out time. Before the freeze-out the number density is well approximate by the equilibrium density, thus an approximate solution is obtained by imposing $\frac{\mathrm{d}\Delta}{\mathrm{d}x} = 0$, which yields

$$\Delta_< \equiv \Delta = -\frac{x^2}{\lambda \left[\Delta + 2Y_{\chi,eq}\right]} \frac{\mathrm{d}Y_{\chi,eq}}{\mathrm{d}x}. \tag{1.13}$$

After the freeze-out $Y_\chi \simeq \Delta$, so

$$\frac{\mathrm{d}\Delta}{\mathrm{d}x} = -\lambda x^{-2} \Delta^2 \tag{1.14}$$

and then

$$Y_\chi^{-1}(x) \simeq \Delta_>^{-1} = -\int_{x_{FO}}^{x} \mathrm{d}x \frac{\lambda}{x^2}. \tag{1.15}$$

It reads today as

$$Y_\chi^0 = -\int_{x_{FO}}^{\infty} \mathrm{d}x \frac{\lambda}{x^2} = \sqrt{\frac{45}{\pi}} \frac{g_*^{1/2}}{g_{*,s}} \frac{1}{m_\chi M_P} \frac{1}{J(x_f)}, \tag{1.16}$$

where

$$J(x_f) = \int_{x_f}^{\infty} \mathrm{d}x \frac{\langle \sigma v \rangle}{x^2} \tag{1.17}$$

and the corresponding matter density parameter is

$$\Omega_\chi h^2 = \frac{1.07 \times 10^9 \mathrm{GeV}^{-1}}{g_*^{1/2} M_P J(x_f)}. \tag{1.18}$$

The cross section results in

$$\langle \sigma v \rangle = \frac{\alpha^2}{32\pi m_\chi^2}. \tag{1.19}$$

Numerical solutions of equation (1.16) for three values of α are shown in Fig. 1.1.

1.1.2 Hot and warm relics

A relic is hot if relativistic at decoupling from the primordial plasma. The freeze-out temperature can be computed as

$$g_{\mathrm{eff}} \frac{\zeta(3)}{\pi^2} T_{FO}^3 \langle \sigma v \rangle = \frac{\pi}{3\sqrt{10}} g_*^{1/2}(T_{FO}) \frac{T_{FO}^2}{M_P} \tag{1.20}$$

and then

$$T_{FO} = \frac{\pi^3}{3\zeta(3)\sqrt{10}} \frac{g_*^{1/2}(T_{FO})}{g_{\mathrm{eff}}} \frac{1}{\langle \sigma v \rangle M_P}. \tag{1.21}$$

In this case it is not necessary to solve the Liouville equation since equation (1.20) can be solved analytically for T_{FO}.

The limit $T_{FO} \gg m_\chi$ is fulfilled if the mass or the annihilation cross section of the DM particles are really small, as for the neutrino. A hot relic with mass below the keV scale would be strongly affected by free-streaming, with consequent lack of fluctuations on small scales, contrary to the observed large-scale structure statistics (see also Fig. 1.8).

Once interactions stops being effective, the comoving dark matter number density is frozen-out and today it reads

$$\begin{aligned} Y_\chi^{FO} &= \frac{n_\chi^{FO}(T_{FO})}{s(T_{FO})} = \frac{n_\chi^{eq}(T_{FO})}{s(T_{FO})} = \\ &= \frac{45\zeta(3)}{2\pi^4} \frac{g_{\mathrm{eff}}}{g_{*s}(T_{FO})} \simeq 0.0026\, g_{\mathrm{eff}} \left(\frac{106.75}{g_{*s}(T_{FO})} \right), \end{aligned} \tag{1.22}$$

a value preserved until today. For $\rho_c = 1.053 \times 10^{-5}\, h^2\, \mathrm{GeV\, cm^{-3}}$ and setting $\rho_\chi(t_0) = m_\chi n_\chi(t_0) = m_\chi Y_\chi^{FO} s(t_0)$, one obtains

$$\Omega_\chi h^2 \simeq 7.6 \times 10^{-4} g_{\mathrm{eff}} \left(\frac{106.75}{g_{*s}(T_{FO})} \right) \frac{m_\chi}{\mathrm{eV}}. \tag{1.23}$$

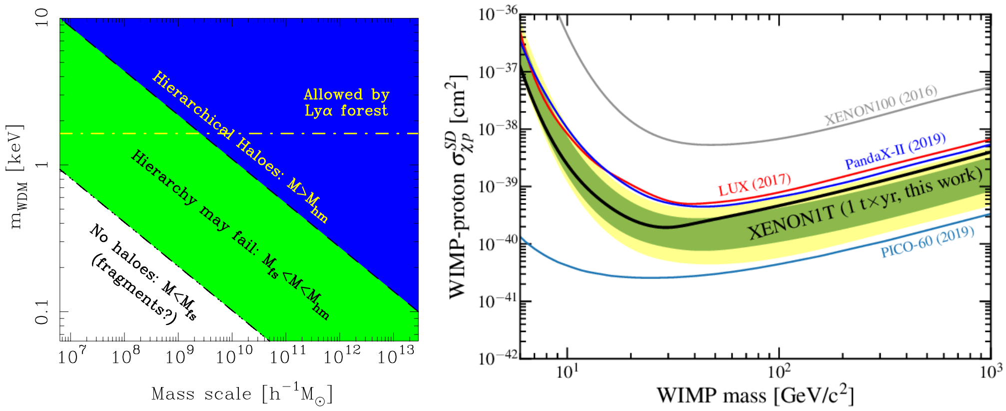

Figure 1.2: (*Right*) Free-streaming mass-scale and half-mode mass scale as a function of the mass of the WDM particle (Schneider et al., 2012). (*Left*) XENON1T 90 percent C.L. upper limit on the spin-dependent WIMP-proton cross section from a 1 ton year exposure. The range of expected sensitivity is indicated by the green (1σ) and yellow (2σ) bands (Aprile et al., 2019).

From the observational measured value $\Omega_\chi h^2 \simeq 0.12$, the bound on dark matter mass (known as the Cowsik-McClennand bound (Cowsik and McClelland, 1972)) is

$$m_\chi \lesssim 1.3\,\mathrm{eV}\frac{1}{g_{\mathrm{eff}}}\left(\frac{g_{*s}(T_{FO})}{106.75}\right), \tag{1.24}$$

where the precise value depends on the value of g_{*s} at decoupling. For slightly massive neutrinos $g_{*s} = 10.75$ and $g_{\mathrm{eff}} = 3/2$, thus $m_\nu \lesssim 10\,\mathrm{eV}$. On the contrary, if the particle decouples at around 300 GeV, then $g_{*s} = 106.75$ and $m_\chi \lesssim 100\,\mathrm{eV}$: the particle will have a very small relic abundance and temperature compared to the photons of the cosmic background. These particles are called *warm relics*.

1.1.3 Constraints on dark matter

The most famous thermal candidates[1] are Weakly Interacting Massive Particles (WIMPs). These candidates are motivated from particle physics and naturally arise in theories addressing the origin of the electroweak scale. Broadly speaking, they have mass and cross section in the following range

$$1\,\mathrm{GeV} \lesssim m_{\mathrm{WIMP}} \lesssim 10\,\mathrm{TeV}, \qquad \sigma_{\mathrm{WIMP}} \simeq 1\,\mathrm{pb}. \tag{1.25}$$

The first interesting constraint on the dark matter nature is given by the considerations exposed in the previous section, and the bounds are reported in Fig. 1.2 (left).The current knowledge about WIMPs can be summed in Fig. 1.2 (right), where the experimental constraints on the WIMPs mass with respect to their cross section are reported.

[1]Dark matter particle candidate which was in thermal equilibrium in the early universe at very high temperature and whose departure from thermal equilibrium is the process that set today relic density.

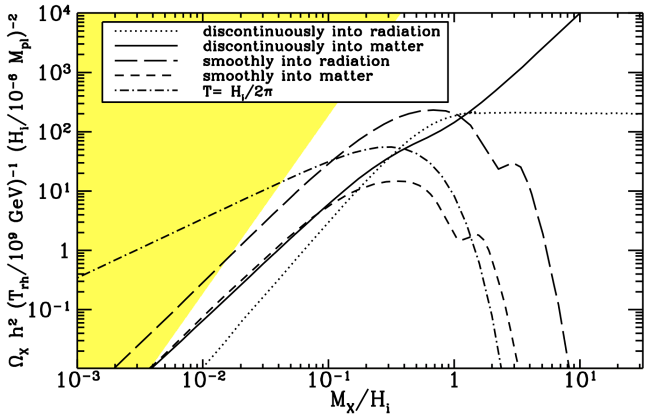

Figure 1.3: The Lee-Weinberg limit (Chung, Kolb, and Riotto, 1999).

A second constraint is the one given by the Lee-Weinberg limit, in Fig. 1.3, that relates the abundance of neutrino or WIMPs to their mass, in order to explain the amount of dark matter measured.

1.2 The post-recombination Universe: structures' formation

During the recombination epoch (e.g. Barkana and Loeb (2001) and Mo, van den Bosch, and White (2010)), around redshift $z \approx 1300$, electrons and protons recombined to form hydrogen atoms. At this time, the Universe was almost completely neutral and very homogeneous, as suggested by the extended Copernican principle in the Cosmic Microwave Background (CMB, see Planck Collaboration et al. (2018) for the latest results). The Universe continued expanding adiabatically, cooling and entering a *dark age*. The CMB temperature decreased with redshift as

$$T_{\rm CMB} = 2.736\,(1+z)\,{\rm K}. \tag{1.26}$$

Due to the expansion of the Universe and to recombination, the recombination rate started to decrease until it became much lower than the expansion rate and the number of free electron was frozen (Fig. 1.4). The fluctuations of the matter density field started growing not linearly, collapsing and forming the first objects. The *dark age* ended when the first stars, quasars and galaxies began to form. Having a radaitive spectrum very energetic, they are responsible for the ionization of the Inter Galactic Medium (IGM).

1.2.1 Linear evolution

After the recombination was almost completely uniform, with spatial energy density fluctuations of the order 10^{-5}. The gravitational instability along with the expansion of

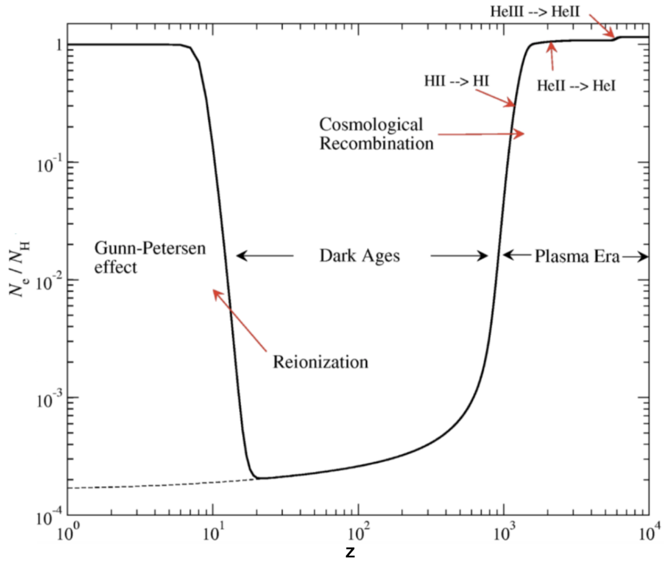

Figure 1.4: Fraction of free-electron density depending on the redshift.

the Universe, allowed the growth of these fluctuations, into the formation of today large scale structure.

Consider the Newtonian theory for the evolution of the density ρ and velocity $\mathbf{u}$ of a non-relativistic fluid under the influence of a gravitational field with potential ϕ. The fluid description is valid as long as the mean free path of the particles in consideration is much smaller than the scale of interest. The fluid description is also valid for a pressure-less dust (i.e. for collision-less dark matter), as long as the local velocity dispersion of the dark matter particles is sufficiently small that particle diffusion can be neglected. The time evolution of a fluid is given by the continuity equation (1.27), the Euler equation (1.28) and the Poisson equation (1.29)

$$\frac{\mathrm{D}\rho}{\mathrm{D}t} = -\rho\nabla_{\mathbf{r}} \cdot \mathbf{u}, \tag{1.27}$$

$$\frac{\mathrm{D}\mathbf{u}}{\mathrm{D}t} = -\frac{\nabla_{\mathbf{r}} P}{\rho} - \nabla_{\mathbf{r}}\phi, \tag{1.28}$$

$$\nabla_{\mathbf{r}}^2\phi = 4\pi G\rho, \tag{1.29}$$

where $\mathbf{r}$ is the proper coordinate and

$$\frac{\mathrm{D}}{\mathrm{D}t} \equiv \frac{\partial}{\partial t} + \mathbf{u} \cdot \nabla_{\mathbf{r}}. \tag{1.30}$$

The comoving coordinated $\mathbf{x}$ is defined as

$$\mathbf{r} = a(t)\mathbf{x} \tag{1.31}$$

and proper velocity $\mathbf{u} = \dot{\mathbf{r}}$ can be written as

$$\mathbf{u} = \dot{a}(t)\mathbf{r} + \mathbf{v}, \qquad \mathbf{v} \equiv a\dot{\mathbf{x}}. \tag{1.32}$$

Writing ρ in terms of the density perturbation contrast against the background,

$$\rho(\mathbf{x},t) = \bar{\rho}(t)[1+\delta(\mathbf{x},t)], \tag{1.33}$$

and using the fact that $\bar{\rho} \propto a^{-3}$, equations (1.27) and (1.29) become

$$\frac{\partial \delta}{\partial t} + \frac{1}{a}\nabla \cdot [(1+\delta)\mathbf{v}] = 0, \tag{1.34}$$

$$\frac{\partial \mathbf{v}}{\partial t} + \frac{\dot{a}}{a}\mathbf{v} + \frac{1}{a}(\mathbf{v}\cdot\nabla)\mathbf{v} = -\frac{\nabla\Phi}{a} - \frac{\nabla P}{a\bar{\rho}(1+\delta)}, \tag{1.35}$$

$$\nabla^2\Phi = 4\pi G\bar{\rho}a^2\delta, \tag{1.36}$$

where $\Phi \equiv \phi + a\ddot{a}x^2/2$ and $\nabla \equiv \nabla_{\mathbf{x}} = a\nabla_{\mathbf{r}}$.

The equation of state of the fluid is determined by the thermodynamic process that the fluid undergoes. In special cases where the pressure of the fluid depends only on the density ρ, the set of fluid equations is completed with the equation of state, $P = P(\rho, S)$, with S the specific entropy. From thermodynamic considerations, it is possible to define the adiabatic sound speed, as

$$c_{\mathrm{s}} = \left(\frac{\partial P}{\partial \rho}\right)_S^{1/2}. \tag{1.37}$$

Thus, the Euler equation (1.35) can be written as

$$\frac{\partial \mathbf{v}}{\partial t} + \frac{\dot{a}}{a}\mathbf{v} + \frac{1}{a}(\mathbf{v}\cdot\nabla)\mathbf{v} = -\frac{\nabla\Phi}{a} - \frac{c_{\mathrm{s}}^2}{a}\frac{\nabla\delta}{(1+\delta)} - \frac{2T}{3a}\nabla S. \tag{1.38}$$

In special cases where both δ and $\mathbf{v}$ are small so that the nonlinear terms can be neglected, one obtains

$$\frac{\partial \delta}{\partial t} + \frac{1}{a}\nabla\cdot\mathbf{v} = 0, \tag{1.39}$$

$$\frac{\partial \mathbf{v}}{\partial t} + \frac{\dot{a}}{a}\mathbf{v} = -\frac{\nabla\Phi}{a}\frac{c_{\mathrm{s}^2}}{a}\nabla\delta - \frac{2\bar{T}}{3a}\nabla S, \tag{1.40}$$

where $\bar{T}$ is the background temperature. Differentiating equation (1.39) and using equations (1.29) and (1.40), the result is

$$\frac{\partial^2\delta}{\partial t^2} + 2\frac{\dot{a}}{a}\frac{\partial\delta}{\partial t} = 4\pi G\bar{\rho}\delta + \frac{c_{\mathrm{s}^2}}{a^2}\nabla^2\delta + \frac{2}{3}\frac{\bar{T}}{a^2}\nabla^2 S. \tag{1.41}$$

In the linear regime, the equations governing the evolution of the perturbations are all linear in perturbation quantities. If the curvature of the Universe can be neglected the mode functions can be chosen to be plane waves and the perturbation fields can be represented by their Fourier transforms. For example,

$$\delta(\mathbf{x},t) = \sum_{\mathbf{k}}\delta_{\mathbf{k}}(t)\exp(i\mathbf{k}\cdot\mathbf{x}), \qquad \delta_{\mathbf{k}}(t) = \frac{1}{V}\int\delta(\mathbf{x},t)\exp(-i\mathbf{k}\cdot\mathbf{x})\mathrm{d}^3\mathbf{x}, \tag{1.42}$$

where V is the volume of a large box in which the perturbations are assumed to be periodic and k is the comoving wavenumber equal to $\frac{2\pi}{\lambda}$. Fourier transforming equation (1.41), one obtains

$$\frac{\mathrm{d}^2\delta_{\mathbf{k}}}{\mathrm{d}t^2} + 2\frac{\dot{a}}{a}\frac{\mathrm{d}\delta_{\mathbf{k}}}{\mathrm{d}t} = \left[4\pi G\bar{\rho} - \frac{k^2 c_{\mathrm{s}^2}}{a^2}\right]\delta_{\mathbf{k}} - \frac{2}{3}\frac{\bar{T}}{a^2}k^2 S_{\mathbf{k}}. \tag{1.43}$$

Pressureless fluid For perturbations in a pressureless fluid, equation (1.43) becomes

$$\frac{\mathrm{d}^2\delta_{\mathbf{k}}}{\mathrm{d}t^2} + 2\frac{\dot{a}}{a}\frac{\mathrm{d}\delta_{\mathbf{k}}}{\mathrm{d}t} = 4\pi G\bar{\rho}_{\mathrm{m}}\delta_{\mathbf{k}}, \tag{1.44}$$

where $\bar{\rho}_{\mathrm{m}}$ is the mean density of the fluid. For non-relativistic (i.e. cold) dark matter this equation admits a generic solution of type $\delta(x,t) = D_+(t)A(x) + D_-(t)B(x)$. If the late-time universe is dominated by a cosmological constant, the decreasing mode is $D_-(t) \propto H(t)$ and the corresponding growing mode is given by

$$D_+(t) \propto \frac{\sqrt{\Omega_\Lambda a^3 + \Omega_k a + \Omega_m}}{a^{3/2}} \int \frac{a^{3/2}\mathrm{d}a}{(\Omega_\Lambda a^3 + \Omega_k a + \Omega_m)^{3/2}}. \tag{1.45}$$

Here the contribution of the radiation field is neglected, as subdominant for $z \ll 10^4$.

The baryonic sound speed varies spatially, so the baryon temperature and density fluctuations must be tracked separately. The evolution of the linear density fluctuations of the dark matter (δ_{dm}) and the baryons (δ_{b}) is described by two coupled second-order differential equations (Naoz and R. Barkana, 2007):

$$\ddot{\delta}_{\mathrm{dm}} + 2H\dot{\delta}_{\mathrm{dm}} = \frac{3}{2}H_0^2\frac{\Omega_m}{a^3}(f_{\mathrm{b}}\delta_{\mathrm{b}} + f_{\mathrm{dm}}\delta_{\mathrm{dm}}) \tag{1.46}$$

$$\ddot{\delta}_{\mathrm{b}} + 2H\dot{\delta}_{\mathrm{b}} = \frac{3}{2}H_0^2\frac{\Omega_m}{a^3}(f_{\mathrm{b}}\delta_{\mathrm{b}} + f_{\mathrm{dm}}\delta_{\mathrm{dm}}) - \frac{k^2}{a^2}\frac{k_B\bar{T}}{\mu}(\delta_{\mathrm{b}} + \delta_{\mathrm{T}}) \tag{1.47}$$

where μ is the mean molecular weight, $\bar{T}$ and δ_{T} are the mean baryon temperature and its dimensionless fluctuation, and f_{b} and f_{dm} the baryon and dark matter mass fractions. Defining $\delta_{\mathrm{tot}} = f_{\mathrm{b}}\delta_{\mathrm{b}} + f_{\mathrm{dm}}\delta_{\mathrm{dm}}$, one obtains

$$\ddot{\delta}_{\mathrm{tot}} + 2H\dot{\delta}_{\mathrm{tot}} = \frac{3}{2}H_0^2\frac{\Omega_m}{a^3}\delta_{\mathrm{tot}} - f_{\mathrm{b}}\frac{k^2}{a^2}\frac{k_B\bar{T}}{\mu}(\delta_{\mathrm{b}} + \delta_{\mathrm{T}}). \tag{1.48}$$

On small scales ($\delta_{\mathrm{b}} \ll [\delta_{\mathrm{tot}}, \delta_{\mathrm{dm}}]$), equation (1.47) becomes

$$\ddot{\delta}_{\mathrm{dm}} + 2H\dot{\delta}_{\mathrm{dm}} \cong f_{\mathrm{dm}}\frac{3}{2}H_0^2\frac{\Omega_m}{a^3}\delta_{\mathrm{dm}}. \tag{1.49}$$

Finally, in the approximation of a uniform sound speed, the evolution of the density fluctuations is described by a different set of coupled second order differential equations:

$$\ddot{\delta}_{\mathrm{dm}} + 2H\dot{\delta}_{\mathrm{dm}} = \frac{3}{2}H_0^2\frac{\Omega_m}{a^3}(f_{\mathrm{b}}\delta_{\mathrm{b}} + f_{\mathrm{dm}}\delta_{\mathrm{dm}}) \tag{1.50}$$

$$\ddot{\delta}_{\mathrm{b}} + 2H\dot{\delta}_{\mathrm{b}} = \frac{3}{2}H_0^2\frac{\Omega_m}{a^3}(f_{\mathrm{b}}\delta_{\mathrm{b}} + f_{\mathrm{dm}}\delta_{\mathrm{dm}}) - \frac{k^2}{a^2}c_{\mathrm{s}}^2\delta_{\mathrm{b}}. \tag{1.51}$$

Perturbations in two non-relativistic components When baryons and pressureless cold dark matter co-exist, density perturbations of baryons induced by a pressureless (cold) dark matter component obeys, as long as the dark matter component is dominating, the equation (in Fourier space):

$$\frac{\mathrm{d}^2\delta_\mathrm{b}}{\mathrm{d}t^2} + 2\frac{\dot{a}}{a}\frac{\mathrm{d}\delta_\mathrm{b}}{\mathrm{d}t} + \frac{k^2 c_{\mathrm{s}^2}}{a^2}\delta_\mathrm{b} = 4\pi G\bar{\rho}_0\frac{a_0^3}{a^3}\delta_\mathrm{dm}, \tag{1.52}$$

where δ_dm is the density perturbations in the dark matter, obey equation (1.44). A solution of this equation is

$$\delta_\mathrm{b}(\mathbf{k}, t) = \frac{\delta_\mathrm{dm}(\mathbf{k}, t)}{1 + k^2/k_\mathrm{J}^2}, \tag{1.53}$$

where

$$k_\mathrm{J}^2 = \frac{3a^2H^2}{2c_\mathrm{s}^2} \tag{1.54}$$

is the Jeans scale.

The statistical properties are given by the variance of the different $\mathbf{k}$-modes, proportional to the power spectrum $P(k)$

$$\langle \delta_\mathbf{k}\delta^*_{\mathbf{k}'}\rangle = (2\pi)^3 P(k)\delta^{(3)}(\mathbf{k} - \mathbf{k}'). \tag{1.55}$$

Different evolution models (concerning the kind of dark matter or the inflaction paradigm, for example) give very different power spectrum, allowing to make strong statements about the nature of the Universe. The power spectrum is indeed a powerful statistical tool, that can give informations about the evolution of structures on large and small scale:

- $k \ll k_\mathrm{J}$: on large scales, it evolves proportionally to the square of the growth factor $D^+(t)$, what is called *linear evolution*;
- $k \gg k_\mathrm{J}$: on small scales, the contribution from non-linear gravitational growth of perturbations becomes more significant and the power spectrum grows *non-linear.*

An estimate for the free-streaming length can be obtained by computing the comoving length scale that a particle may travel up until matter-radiation equality (t_EQ). The Jeans length drops dramatically and perturbations may collapse under gravity. From Kolb and Turner (1990), one obtains

$$\lambda_\mathrm{fs} = \int_0^{t_\mathrm{EQ}} \frac{v(t)dt}{a(t)} \approx \int_0^{t_\mathrm{NR}} \frac{cdt}{a(t)} + \int_{t_\mathrm{NR}}^{t_\mathrm{EQ}} \frac{v(t)dt}{a(t)} \tag{1.56}$$

where t_NR is the epoch when the WDM particles become non-relativistic, which occurs when $T_\mathrm{WDM} < m_\mathrm{WDM}c^2/3k_\mathrm{B}$, where T_WDM and m_WDM are the characteristic temperature and mass of the WDM particles. In the non-relativistic regime, it yields to

$$\lambda_\mathrm{fs} \approx r_\mathrm{H}(t_\mathrm{NR})\left[1 + \frac{1}{2}\log\frac{t_\mathrm{EQ}}{t_\mathrm{NR}}\right] \approx 0.4\left(\frac{m_\mathrm{WDM}}{\mathrm{keV}}\right)^{-4/3}\left(\frac{\Omega_\mathrm{WDM}h^2}{0.135}\right)^{1/3}\mathrm{Mpc}. \tag{1.57}$$

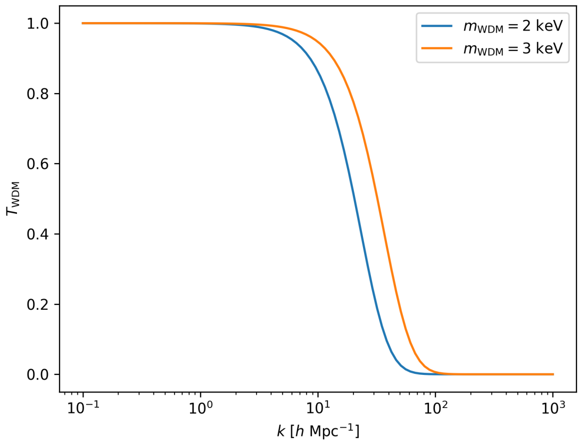

Figure 1.5: Transfer function computed according to equation (1.58), for two values of WDM masses. Here $\Omega_{\rm WDM} = 0.269$ according to Carucci et al. (2015).

However, the fluctuations inside the horizon grow logarithmically during radiation domination and free-streaming does not switch off immediately after $t_{\rm EQ}$. About the WDM density transfer function, following Viel et al. (2005) and Bode, Ostriker, and Turok (2001) one obtains

$$T_{\rm WDM}(k) = \left[\frac{P_{\rm lin}^{\rm WDM}}{P_{\rm lin}^{\rm CDM}}\right]^{1/2} = \left[1 + (\alpha k)^{2\mu}\right]^{-5/\mu}, \tag{1.58}$$

with $\mu = 1.12$ and

$$\alpha = 0.049 \left[\frac{m_{\rm WDM}}{\rm keV}\right]^{-1.11} \left[\frac{\Omega_{\rm WDM}}{0.25}\right]^{0.11} \left[\frac{h}{0.7}\right]^{1.22} {\rm h}^{-1}\,{\rm Mpc}. \tag{1.59}$$

The transfer function for $m_{\rm WDM} = 2$, 3 keV is shown in Fig. 1.5. The steep dumping from $k \approx 10^1\,h^{-1}$Mpc to $k \approx 10^2\,h^{-1}$Mpc of the transfer function and consequently of the WDM power spectrum reflect the lack of structure below scales of $r = 2\pi/k \approx 1\,h^{-1}$ Mpc. The masses of sterile neutrino WDM particles m_{ν_s} can be obtained from $m_{\rm WDM}$ through

$$m_{\nu_s} = 4.43{\rm keV}\left(\frac{\rm m_{WDM}}{\rm 1keV}\right)^{4/3}\left(\frac{\Omega_{\rm WDM}}{0.1225}\right)^{-1/3}. \tag{1.60}$$

The effective free-streaming length is defined as $\lambda_{\rm fs}^{\rm eff} \equiv \alpha$ and the free-streaming mass is

$$M_{\rm fs} = \frac{4\pi}{3}\bar{\rho}\left(\frac{\alpha}{2}\right)^3. \tag{1.61}$$

The half-mode length is instead the length scale at which the amplitude of the WDM transfer function is reduced by half:

$$\lambda_{\rm hm} = 2\pi\alpha(2^{\mu/5} - 1)^{-1/2\mu} \approx 13.93\alpha \tag{1.62}$$

and the corresponding mass is

$$M_{\rm hm} = \frac{4\pi}{3}\bar{\rho}\left(\frac{\lambda_{\rm hm}}{2}\right)^3 \approx 2.7\times 10^3 M_{\rm fs}. \tag{1.63}$$

The normalization (amplitude) of the power spectrum is not predicted by any current theory of cosmic perturbation, so it has to be fixed by observations. The prescription used depends on the variance of the galaxy distribution. These quantities are related by:

$$\sigma^2(R,z) = \frac{1}{2\pi^2}\int P(k,z)\widetilde{W}_R^2(k)k^2\mathrm{d}k, \tag{1.64}$$

where

$$P(k,z) = D_+^2(z)P(k,0), \tag{1.65}$$

and $\widetilde{W}$ is the Fourier transform of a window function W. For the top-hat window function,

$$W_R(r) = \begin{cases} \left(\frac{4\pi}{3}R^3\right)^{-1} & \text{if } r\leq R, \\ 0 & \text{otherwise,}\end{cases} \tag{1.66}$$

where R is a comoving radius and one has

$$\widetilde{W}_R(k) = \frac{3}{(kR)^3}\left[\sin(kR) - kR\cos(kR)\right]. \tag{1.67}$$

The window size can be label by the mean mass contained in it:

$$M(R) \equiv \overline{\rho}(t_0)\frac{4\pi}{3}R^3, \tag{1.68}$$

where $\overline{\rho}$ is the mean density of the Universe, conventionally measured at present-day, $\bar{\rho}(t_0)\equiv\rho_0$. The normalization of the amplitude of the power spectrum is often specified by the value of $\sigma_8 \equiv \sigma(R = 8h^{-1}\mathrm{Mpc})$ (e.g. $\sigma_8 = 0.8159$ from Planck Collaboration (2016)), consistent with the specifics of the simulations used in Chapter 2. In Fig. 1.6, the power spectrum in obtained using equation (1.65) and with the `CAMB` code (Lewis and Challinor, 2011).

The structure formation in cold dark matter models proceeds hierarchically: at early times, the majority of dark matter is situated in low-mass haloes and high-mass haloes are formed from the merging of the former.

In Fig. 1.8 the difference in the large scale structure evolution for different models is shown: while the difference between cold dark matter (*left*) and warm dark matter with an intermediate mass ($m_p = 1\,\mathrm{keV}$, *center*) is not immediately visible, the WDM effects are prominent in the *right* panel, where $m_p = 0.25\,\mathrm{keV}$.

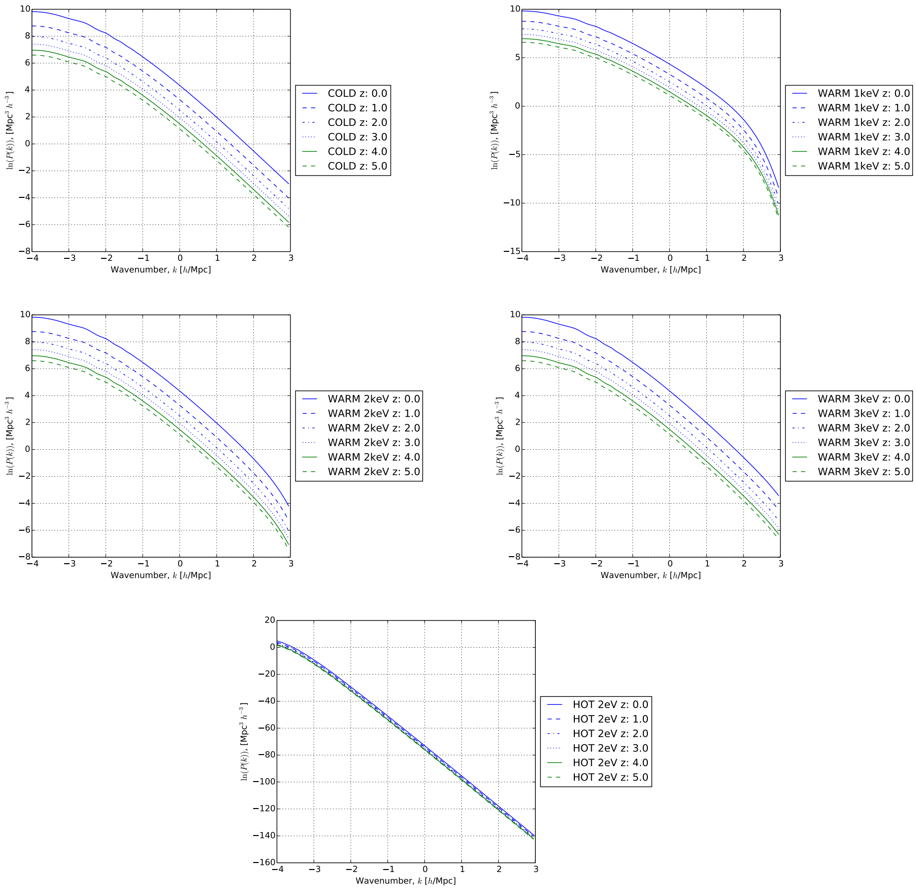

Figure 1.6: Power spectrum for $0 \leq z \leq 5$.

Non-linear evolution: spherical collapse and halo mass function

A non-linear description of the evolution of the Universe is necessary as soon as the matter density become of order unity. The dynamics of dark matter collapse can be exactly solved only in some specific symmetry (e.g. spherical symmetry) and for regions (smaller than the Hubble horizon $cH^{-1}(z)$). Considering an initial times t_i top-hat of uniform overdensity δ_i inside a sphere of radius R, the formation of an halo can been analyze in a Newtonian context:

$$\ddot{r} = -\frac{GM}{r^2} - \frac{4\pi G}{3}(\rho + 3p)_{\mathrm{rest}} r, \tag{1.69}$$

considering all the matter that does not participate in the collapse. Being r_{dm} and r_{b} the physical radii that enclose a fixed mass of dark matter and of baryons, we obtain two coupled non-linear equations of motion:

$$\ddot{r}_{\mathrm{dm}} = -\frac{1}{r_{\mathrm{dm}}^2}\frac{4\pi G}{3} r_{\mathrm{dm}}^3(\rho_{\mathrm{dm}} + \rho_{\mathrm{b}}) + H_0^2\Omega_\Lambda r_{\mathrm{dm}} - \frac{8\pi G}{3}\rho_{\mathrm{r}} r_{\mathrm{dm}}, \tag{1.70}$$

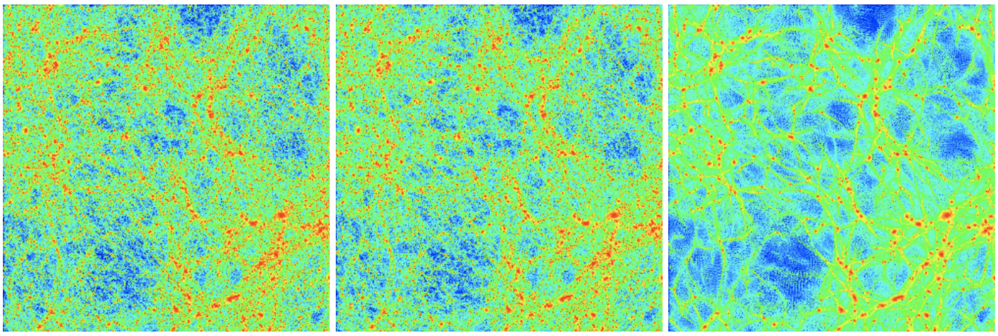

Figure 1.7: Density maps from simulations with a length of $L = 25\,h^{-1}$Mpc at $z = 1.1$. From left to right: CDM, WDM with $m_p = 1$ keV and WDM with $m_p = 0.25$ keV. The WDM effects are prominent in the last one, where the voids are noticeably emptier than in CDM (Schneider et al., 2012).

$$\ddot{r}_{\mathrm{b}} = -\frac{1}{r_{\mathrm{b}}^2}\frac{4\pi G}{3}r_{\mathrm{b}}^3(\rho_{\mathrm{dm}} + \rho_{\mathrm{b}}) + H_0^2\Omega_\Lambda r_{\mathrm{b}} - \frac{8\pi G}{3}\rho_{\mathrm{r}} r_{\mathrm{b}}. \tag{1.71}$$

Since the time when the fluctuation enters the horizon is substantially early in the radiation- dominated universe, the baryon-photon coupling yields δ_{b}, $\delta_\gamma \ll \delta_{\mathrm{dm}}$, δ_{tot} initially. The resulting critical (linear) ovendensity at the time of collapse in shown in Fig.

The overdensities star growing linearly, as $\delta_L = \delta_i \frac{D_+(t)}{D_+(t_i)}$, until it reaches a radius of maximum expansion and it collapses. The corresponding δ (equation (1.33)) is called δ_c and it is given by (Henry, 2000)

$$\delta_c(z) = \frac{3\,(12\pi)^{\frac{2}{3}}}{20}\,(1 + 0.0123\log_{10}\Omega_m(z)) \tag{1.72}$$

with

$$\Omega_m(z) = \Omega_{m,0}\,(1+z)^3\,\frac{\rho_{c,0}}{\rho_c(z)} = 0.308\,(1+z)^3\left(\frac{H_0}{H(z)}\right)^2, \tag{1.73}$$

where

$$\rho(z) = \frac{3\,H(z)^2}{8\pi G}. \tag{1.74}$$

The symmetry of the initial perturbation would yield in the evolution of the halo to a singularity, the halo indeed reaches a state of virial equilibrium by violent relaxation. The final overdensity relative to the critical density at the collapse redshift can be obtained using the virial theorem. The critical overdensity at collapse will be

$$\Delta_{\mathrm{c}} = \frac{\rho_{\mathrm{coll}}}{\rho_b} = (1 + \delta_{\mathrm{coll}}) \approx 18\pi^2 \approx 178 \tag{1.75}$$

in Einstein-de Sitter model and

$$\Delta_c = 18\pi^2 - 82d - 39d^2 \tag{1.76}$$

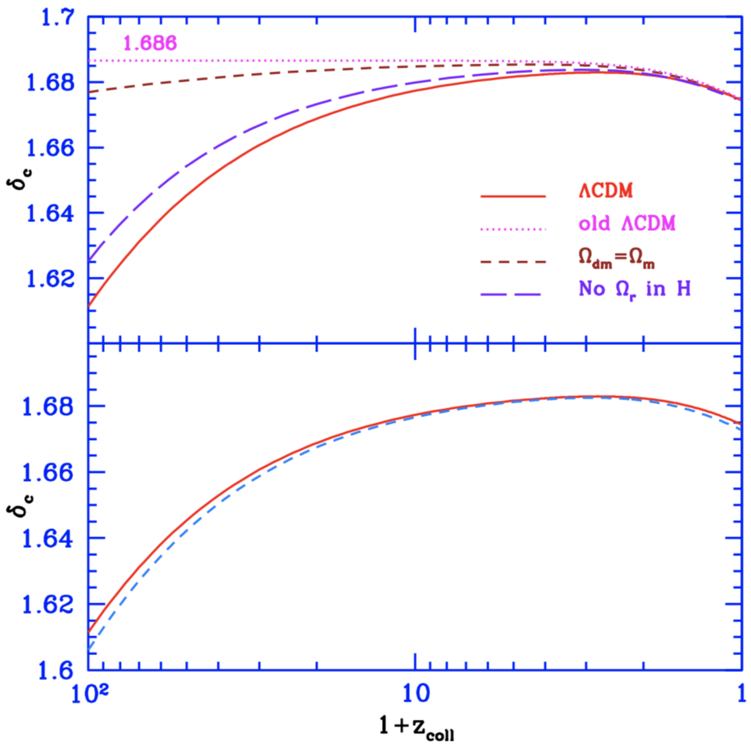

Figure 1.8: Critical overdensity versus collapse redshift. It is compared δ_c for the full calculation (solid curves) to the results with other assumptions. The top panel compares to several cases that include only some of the physical ingredients that affect the spherical collapse calculation. The bottom panel shows results also for the Viel et al. (2005) set of parameters (dashed curve). From Naoz and R. Barkana (2007).

with

$$d \equiv \Omega_m(z) - 1 \tag{1.77}$$

$$\Omega_m(z) = \frac{\Omega_{m,0}(1+z)^3}{\Omega_{m,0}(1+z)^3 + \Omega_{\Lambda,0} + \Omega_{k,0}(1+z)^2} \tag{1.78}$$

for a ΛCDM cosmology. The critical overdensity define the virial radius

$$r_{\rm vir} = 0.784 \left(\frac{M}{10^8 h^{-1} M_\odot}\right)^{1/3} \left[\frac{\Omega_{m,0}}{\Omega_m(z)}\frac{\Delta_c}{18\pi^2}\right]^{-1/3} \left(\frac{1+z}{10}\right)^{-1} h^{-1}\,\mathrm{kpc}, \tag{1.79}$$

and the circular velocity $V_c = (G\,M)^{1/2}\, r_{\rm vir}^{-1/2}$. One can therefore deduce the virial temperature as totally defined by the kinetics of the structure

$$T_{\rm vir} = \frac{\mu\, m_p V_c^2}{2\mathrm{k_B}} = 1.98\times10^4 \left(\frac{\mu}{0.6}\right)\left(\frac{M}{10^8 h^{-1} M_\odot}\right)^{2/3}\left[\frac{\Omega_{m,0}}{\Omega_m(z)}\frac{\Delta_c}{18\pi^2}\right]^{1/3}\left(\frac{1+z}{10}\right)\mathrm{K}, \tag{1.80}$$

with m_p the proton mass and μ the mean molecular weight that depends on the ionization fraction ($\mu = 0.59$ for fully ionized primordial gas, $\mu = 0.61$ for a mixture of ionized hydrogen with singly ionized helium, $\mu = 1.22$ for neutral primordial gas).

The baryon overdensity is closely related to the virial temperature $T_{\rm vir}$ through the relation (Barkana and Loeb, 2001)

$$\delta_b = \frac{\rho_b}{\bar{\rho}_b} - 1 = \left(1 + \frac{6}{5}\frac{T_{\rm vir}}{\bar{T}}\right)^{3/2} - 1 \tag{1.81}$$

where $\bar{T}$ is the background gas temperature. One can deduce the minimum halo mass for baryonic objects, which is close to the Jeans mass if $\delta > 100$ and so $T_{\rm vir} \geqslant 2.9 \times 10^3[(1+z)/100]^2$ K (see Figure 1.10).

The simplest statistics for cosmic structures is the abundance of haloes described by the so-called mass function, i.e. the number density of haloes per unitary mass. The first and simpler analytic model, developed by Press and Schechter (1974), is based on a filtered Gaussian random field of density perturbations linearly growing and becoming non-linear according to the spherical collapse model, i.e. as soon as $\delta(R) > \delta_{sc}$ (equation (1.72)). The result is

$$\frac{\mathrm{d}n}{\mathrm{d}\ln M} = 2\frac{\rho_m}{M}\frac{\mathrm{d}}{\mathrm{d}\ln M}\,\mathrm{erfc}\left(\frac{\nu}{\sqrt{2}}\right) = \sqrt{\frac{2}{\pi}}\frac{\rho_m}{M}\frac{\mathrm{d}\ln\sigma^{-1}}{\mathrm{d}\ln M}\nu\exp\left(-\frac{\nu^2}{2}\right), \tag{1.82}$$

where

$$\nu = \frac{\delta_{sc}(z)}{\sigma(M,z)} \tag{1.83}$$

accounts for the density threshold in units of the rms-variance (equation (1.64)). A better model accounting for the ellipsoidal collapse remark the multiplicative fudge factor 2 solving the cloud-in-cloud problem (Jedamzik, 1995), Sheth and Tormen (1999) is used in this thesis because it is easily generalizable to WDM and HDM cosmologies. The original expression for CDM is

$$\frac{\mathrm{d}n}{\mathrm{d}\ \ln M} = \frac{\bar{\rho}}{M}\frac{\mathrm{d}\ \ln\sigma^{-1}}{\mathrm{d}\ \ln M}\frac{2A}{\nu}\left(1 + \frac{1}{\nu'^{2q}}\right)\left(\frac{\nu'^2}{2\pi}\right)^{1/2}\exp\left(-\frac{\nu'^2}{2}\right) \tag{1.84}$$

where $\nu' = \sqrt{a}\nu$, $a = 0.707$, $q = 0.3$ and $A \approx 0.322$. In Fig. 1.9, the Sheth Tormen mass function is shown for different redshifts. Other models will be considered, such as Watson et al. (2013) and Despali et al. (2016).

In the same way, in Sheth, Mo, and Tormen (2001) the large scale halo-to-mass is defined as

$$b(\nu) = 1 + \frac{1}{\sqrt{a}\delta_{sc}}\left[\sqrt{a}(a\nu^2) + \sqrt{a}b(a\nu^2)^{1-c} - \frac{(a\nu^2)^c}{(a\nu^2)^c + b(1-c)(1-c/2)}\right], \tag{1.85}$$

where the best esteem for the parameters a, b, c is $a = 0.707, b = 0.5, c = 0.6$, and ν is the one defined in equation (1.83).

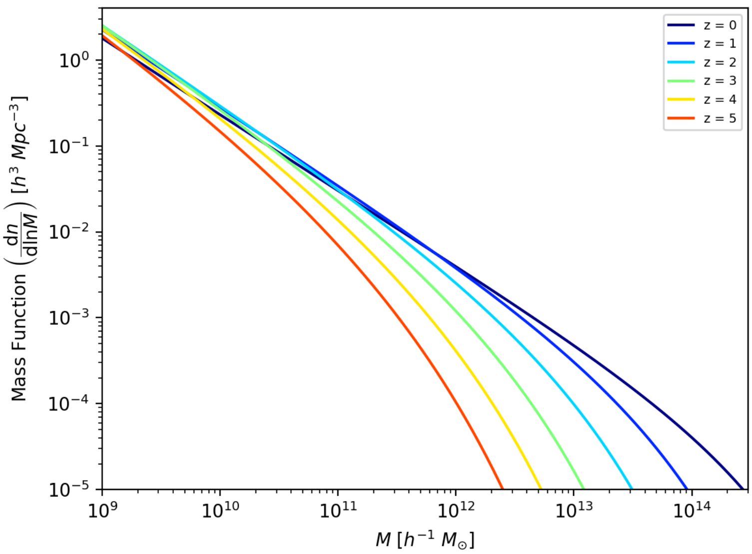

Figure 1.9: Sheth-Tormen mass function for $z \in [0, 5]$.

1.2.2 Reionization process

The reionization of the universe is a complex process starting about 100 million years after Big Bang and covering about 1 Gyr that depends on the radiation field and the atomic and molecular species that fill the particle horizon.

Before the production of metals, the most abundant molecule was the molecular hydrogen H_2; the primary formation processes were

$$\mathrm{H} + \mathrm{e}^- \rightarrow \mathrm{H}^- + h\nu, \tag{1.86}$$

$$\mathrm{H}^- + \mathrm{H} \rightarrow \mathrm{H}_2 + \mathrm{e}^-. \tag{1.87}$$

Molecular hydrogen is quite fragile and it can be photo-dissociated by photons with energies larger than 13.6 eV, to which the IGM was transparent before it is ionized. The UV flux capable of dissociating H_2 throughout the collapsed environments in the universe is lower than the minimum flux necessary to ionize the atomic hydrogen; after the beginning of star formation process, the formation of additional stars due to H_2 cooling is suppressed. A further fragmentation is possible only in objects with a virial temperature higher than 10^4 K. The evolution in redshift is described in Fig. 1.10 (top-pannel): low-mass objects collapse creating ionized hydrogen (HII) bubbles, but the formation of new objects is delayed until H_2 is dissociated and objects with $T_{vir} \geqslant 10^4$ K collapse. This is the beginning of the reionization epoch.

The reionization epoch is divided into three main stages, shown in Fig. 1.10 and 1.11:

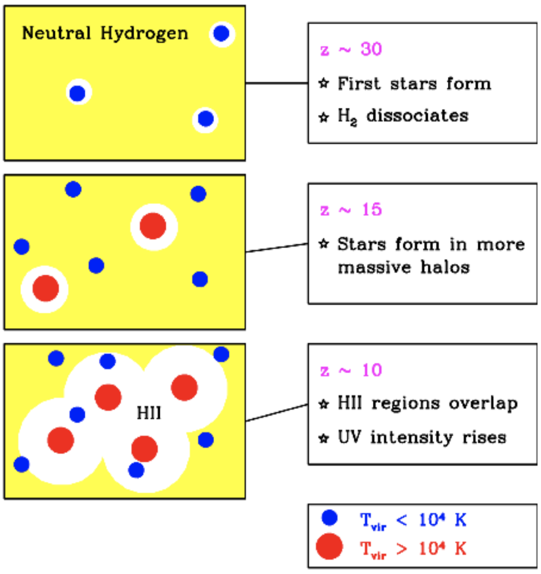

Figure 1.10: Stages in the reionization of hydrogen in the IGM.

- $z \geq 30$: this is the *pre-overlap* phase, in which the Universe is mostly neutral except for isolated HII regions produced by individual ionizing sources that turn on and ionize their surroundings. Although the nature of these sources is an open research field in astrophysics, the main candidates are quasars, young galaxies and Population III stars. The ionizing photons propagate through the high-density regions surrounding with high recombination rate; emerging from these regions, the ionization front can propagate with no difficulties into the low-density regions, leaving behind haloes of neutral gas (Figure 1.10, top panel).

- $15 \lesssim z \lesssim 30$: in the second, central stage the individual HII regions start to *overlap*, leaving the IGM partially ionized and partially neutral. The overlap between near HII regions increase the ionizing intensity, allowing these regions to expand into high-density gas. This phase can be seen as a rapid phase transition (about 0.172 Gyrs in Planck cosmology), lasting less than an Hubble time. The end of this stage is marked by a state in which neutral regions are located inside self-shielded, high-density clouds where the ionizing radiation can not enter, while the low-density IGM is highly ionized (Figure 1.10, middle panel).

- $5 \lesssim z \lesssim 15$: during the last *post-overlap* phase the Universe is almost completely ionized, with only a small neutral fraction. As galaxy formation proceeds, the high-density regions are more and more ionized, but collapsed object retain neutral gas even at present time. Nevertheless, below $z \approx 1.6$, all ionizing sources are visible from every point in the IGM; above this redshift, absorption by Lyman$-\alpha$ forest clouds makes only a few number of sources visible from every point in the IGM (Figure 1.10, bottom panel).

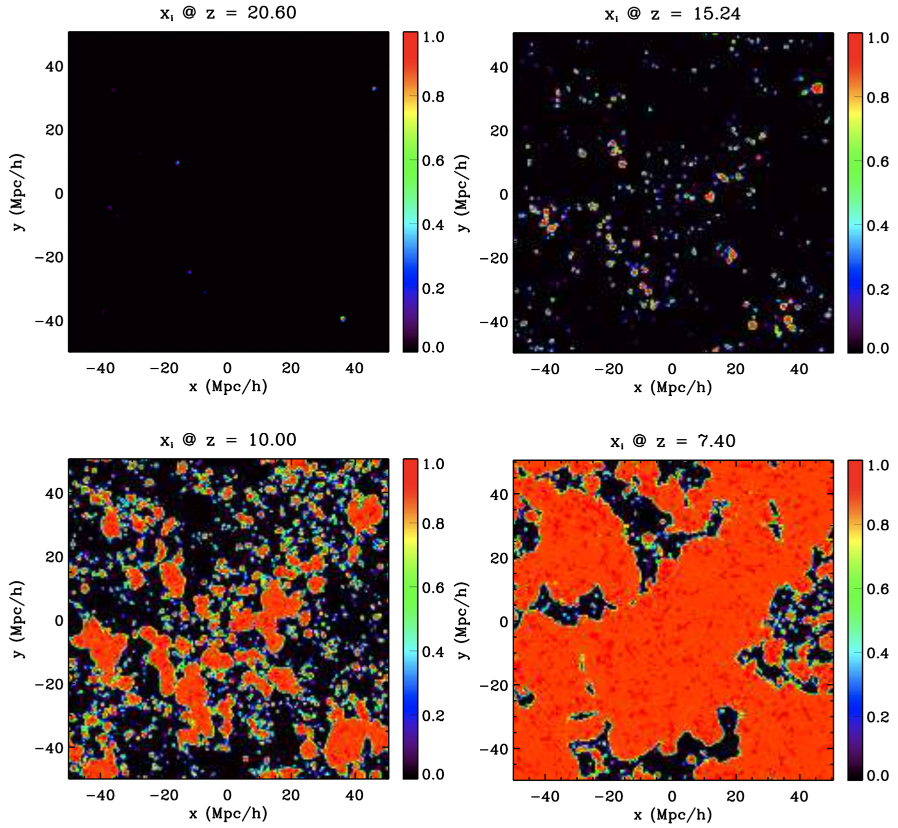

Figure 1.11: Maps of the ionization fraction from simulation (Santos et al., 2008) at redshifts z = 20.60, 15.24, 10.00, 7.40. To be noted the clear separation between the highly ionized regions (in red) and the mostly neutral IGM (black).

Studying this epoch, or more specifically the post-reionization epoch, is possible thanks to the 21cm emission line, which allows to distinguish and look at different epochs using the appropriate frequency. Indeed, a rest-frame wavelength $\lambda_0 = 21\,\mathrm{cm}$ emitted by a source at redshift z corresponds to a frequency $\nu(z) = \nu_0/(1+z)$ with $\nu_0 = c/\lambda_0 = 1420\,\mathrm{MHz}$.

Hydro-dynamical simulations that involve also radiative transport are necessary to describe structure formations (e.g. Ciardi, Stoehr, and White (2003), Pawlik, Schaye, and Dalla Vecchia (2015) and Aubert, Deparis, and Ocvirk (2015)).

1.3 The 21 cm line

The first radio waves originated from an astronomical object were unexpectedly detected in 1932 by Karl Jansky in an attempt to study short wave transmissions. The signal was coming from the Milky Way and soon the radio emissions from stars, galaxies, quasars and pulsars allowed to map the Milky Way and to study the radio emission from the Sun (Jansky, 1982). The main discover for cosmology was made in 1964, again by chance, by Penzias and Wilson: the cosmic microwave background (CMB) radiation. The 21cm line characteristic of neutral hydrogen was first detected in 1951 by Ewen and Purcell at Harvard University (Ewen and Purcell, 1951) and in 1952 the first maps of the neutral hydrogen distribution in the Galaxy were presented: for the first time the spiral structure of the Milky Way was revealed. The first review on this topic by George Field appeared in 1958 (Field, 1958).

The 21cm is a transition between the two hyperfine states of the $1^2S_{1/2}$ ground level of hydrogen. The hyperfine interaction between proton and electron is induced by the coupling between the proton and electron spins, respectively $\vec{I}$ and $\vec{s}$, as usual described by the interaction hamiltonian (in natural units)

$$\begin{aligned} \mathcal{H} = -\vec{\mu}_p \cdot \vec{B} &= -\left(\frac{g_p e}{2m_p}\vec{I}\right) \cdot \left(\frac{8\pi}{3}\vec{\mu}_e \Psi_0^2\right) \\ &= -\left(\frac{g_p e}{2m_p}\vec{I}\right) \cdot \left(-\frac{8\pi}{3}\frac{g_e e}{2m_e}\Psi_0^2 \vec{s}\right) = \\ &= \frac{16\pi}{3}\left(\frac{e}{2m_e}\right)^2 \frac{m_e}{m_p} g_p \Psi_0^2 \, \vec{I} \cdot \vec{s}. \end{aligned} \tag{1.88}$$

being $g_e = 2$. The total angular momentum $\vec{F}$ is the sum of the two spins,

$$\vec{F} = \vec{I} + \vec{s}, \tag{1.89}$$

so the coupling reads

$$\vec{I} \cdot \vec{s} = \frac{1}{2}\left(F^2 - I^2 - s^2\right). \tag{1.90}$$

Being both s and I equal to $\frac{1}{2}$, F is 0 or 1, splitting the ground level into a hyperfine doublet. The $F = 1$ state corresponds to a proton and an electron with parallel spin (i.e. maximum energy), and split into three components in an external magnetic field; it is therefore called *triplet* state. The $F = 0$ state accounts for a configuration with anti-parallel spins (i.e. minimum energy), not spliting in an external magnetic field; it is called *singlet* state. The transition $(F = 1) \to (F = 0)$ is equivalent to a *spin-flip* of the electron with respect to the proton, with the energy levels separated by $\Delta E = h\nu = 5.9 \times 10^{-6}$ eV, a wavelength of 21cm or a frequency of 1420 MHz (in vacuum).

This line has been used to probe of the hydrogen gas along the line-of-sight to some background radio source. from a macroscopic point-of-view, the emission and absorption processes are accounted for the radiative transfer through gas; in a collisionless approximation, for an intensity I_ν, along a path described by coordinate s,

$$\frac{\mathrm{d}I_\nu}{\mathrm{d}s} = -\alpha_\nu I_\nu + j_\nu \tag{1.91}$$

where α_ν and j_ν are the absorption the emission coefficients. Since the photon frequencies ν are smaller than the peak frequency of the CMB ($\nu_{\rm CMB} = 160.23\,{\rm GHz}$), the Rayleigh-Jeans approximation holds. Defining the brightness temperature

$$T = \frac{I_\nu\, c^2}{2k_B \nu^2} \tag{1.92}$$

and the optical depth along the line-of-sight as

$$\tau_\nu = \int {\rm d}s\, \alpha_\nu(s), \tag{1.93}$$

The solution of equation (1.91) reads

$$T_b^{\rm obs} = T_{\rm ex}\,(1 - e^{-\tau_\nu}) + T_{\rm R}(\nu)\, e^{-\tau_\nu}. \tag{1.94}$$

in which $T_{\rm R}$ is the temperature of a background radio source and $T_{\rm ex}$ is the uniform temperature of a cloud with τ_ν.

The excitation temperature of the 21cm line, called the *spin temperature* T_S, is defined by the relative number densities of hydrogen atoms in the two hyperfine levels n_0 (singlet level) and n_1 (triplet level)

$$\frac{n_1}{n_0} = \frac{g_1}{g_0} \exp\left(-\frac{T_\star}{T_S}\right), \tag{1.95}$$

with $T_\star \equiv hc/k_{\rm B}\lambda_{21} = 0.068\,{\rm K}$.

The optical depth of a cloud of hydrogen is

$$\tau_\nu = \int {\rm d}s \left[1 - \exp\left(-\frac{\Delta E}{k_B T_S}\right)\right] \sigma_0 \phi(\nu) n_0 \tag{1.96}$$

where $n_0 = \frac{n_H}{4}$, $\sigma(\nu) = \sigma_0\phi(\nu)$ is the 21 cm cross section with $\sigma_0 \equiv \frac{3c^2 A_{10}}{8\pi\nu^2}$ accounting for the spontaneous decay rate of the spin-flip transition vita the Einstein coefficient $A_{10} = 2.85\times10^{-15}\,{\rm s}^{-1}$ and $\phi(\nu)$ the normalized line profile ($\int \phi(\nu){\rm d}\nu = 1$). To evaluate equation (1.96), a form for $s(\nu)$ has to be chosen, in order to determine the range of frequencies ${\rm d}\nu$ over the path ${\rm d}s$ that correspond to a fixed observed frequency $\nu_{\rm obs}$. This can be done by relating the path length to the cosmological expansion ${\rm d}s = -c{\rm d}z/(1+z)H(z)$ and the redshifting of light to relate the observed and emitted frequencies $\nu_{\rm obs} = \nu_{\rm em}/(1+z)$ (Pritchard and Loeb, 2012).

The differential brightness temperature is (Pritchard and Loeb, 2012)

$$\begin{aligned} \delta T_b &= \frac{T_S - T_R}{1+z}(1 - \exp(-\tau_\nu)) \\ &\approx \frac{T_S - T_R}{1+z}\tau \\ &\approx 27 x_{\rm HI}\,(1+\delta_b)\left(\frac{\Omega_b h^2}{0.023}\right)\sqrt{\frac{0.15}{\Omega_m h^2}\frac{1+z}{10}}\left[\frac{T_S - T_R}{T_S}\right]\frac{\partial_r v_r}{(1+z)H(z)}{\rm mK} \end{aligned} \tag{1.97}$$

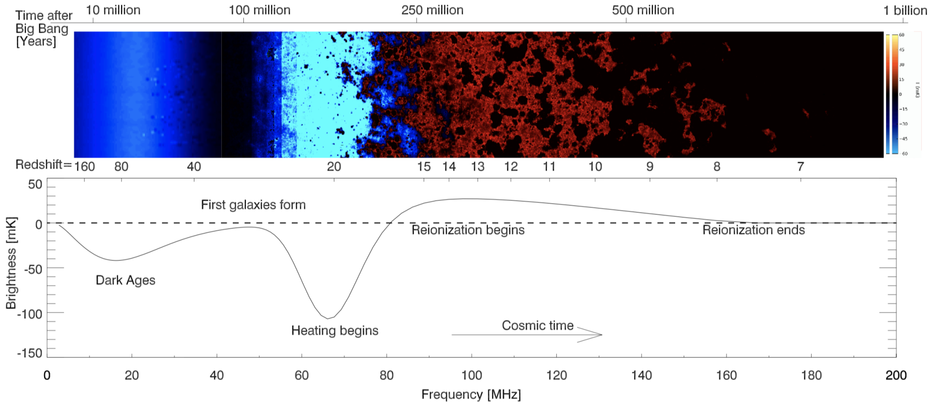

Figure 1.12: Time evolution of fluctuations in the 21cm brightness from the beginning of stars formation to the end of the reionization epoch; the absorption phase of the 21cm radiation is indicated in blue, the emission in red. The evolution of the brightness temperature is also reported. From Pritchard and Loeb (2012).

where $x_{\rm HI}$ is the neutral fraction of hydrogen, δ_b is the fractional overdensity in baryons, and $\partial_r v_r$ is the velocity gradient along the line of sight.

The detectability of the signal depends on the value of the term $[\cdots]$, i.e. the relative difference between the value of the spin temperature and the CMB temperature. Three cases are possible:

- $T_S > T_R$: emission, $\delta T_b > 0$;
- $T_S = T_R$: no signal, $\delta T_b = 0$;
- $T_S < T_R$: absorption, $\delta T_b < 0$.

The evolution of the brightness temperature is described in Fig. 1.12.

The spin temperature results from three processes: the interaction of the 21 cm photons with the CMB photons; hydrogen atoms collisions with other particles (mainly electrons and hydrogen atoms itself); the spin-flip caused by Lyα photons ($2P \to 1S$). The equilibrium between these effect gives the spin temperature:

$$T_S = \frac{1 + x_\alpha + x_c}{\dfrac{1}{T_\gamma} + \dfrac{x_\alpha}{T_\alpha} + \dfrac{x_c}{T_c}}. \tag{1.98}$$

T_γ is the CMB mean temperature, T_α the temperature of the Lyα radiation, T_K is the gas kinetic temperature, closely coupled with T_α by recoil during repeated scattering, x_c the coupling coefficient regarding atomic collisions and $x_\alpha$the coupling coefficient due to the scattering of Lyα photons. More specifically:

- Atomic collisions (hydrogen-hydrogen, HH; hydrogen-proton, Hp; hydrogen-electron, He) may induce spin-flip in hydrogen and dominate the coupling in the early Uni-

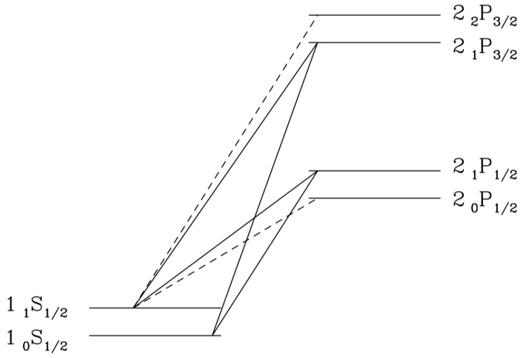

Figure 1.13: Hyperfine structure of the $2P$ and $1S$ level of the hydrogen atom (J. R. Pritchard and Furlanetto, 2006).

verse when the gas density was large. One has

$$x_c^i \equiv \frac{C_{10}}{A_{10}} \frac{T_\star}{T_\gamma} \tag{1.99}$$

with $i =$ HH, Hp, He and C_{10} the collision rate inducing $1 \to 0$ transition. During the cosmic dark ages the coupling is dominated by collisions, which can lead to a suppression of the 21 cm signal by about 5 percent.

- A second channel of coupling is given by the resonant scattering of Lyα photons, a process known as Wouthuysen-Field effect (Field, 1958), illustrated in Fig. 1.13. An hydrogen in the singlet state can be excited into one of the central $2P$ hyperfine states by the absorption of a Lyα photon. Once the Lyα photon is re-emitted, this has access to the levels $1_1 S_{1/2}$ and $1_0 S_{1/2}$ of the two ground state hyperfine levels; if the transition occurs to the triplet state, then a spin-flip occurs. The coupling coefficient is

$$x_\alpha = \frac{4}{27} \frac{P_\alpha T_\star}{A_{10} 1, T_\gamma} \tag{1.100}$$

with P_α the scattering rate of Lyα photons

$$P_\alpha = \int \mathrm{d}\Omega \int \frac{J_\nu}{h\nu} \sigma_\nu \mathrm{d}\nu \tag{1.101}$$

and σ_ν the Ly-α absorption cross-section.

1.4 Intensity mapping techniques

Line-Intensity Mapping (IM) uses the integrated emission from spectral lines in galaxies and the diffuse intergalactic medium to track the growth and evolution of cosmic structure (Kovetz et al., 2017). Instead of focusing on a single galaxy (see Fig. 1.14),

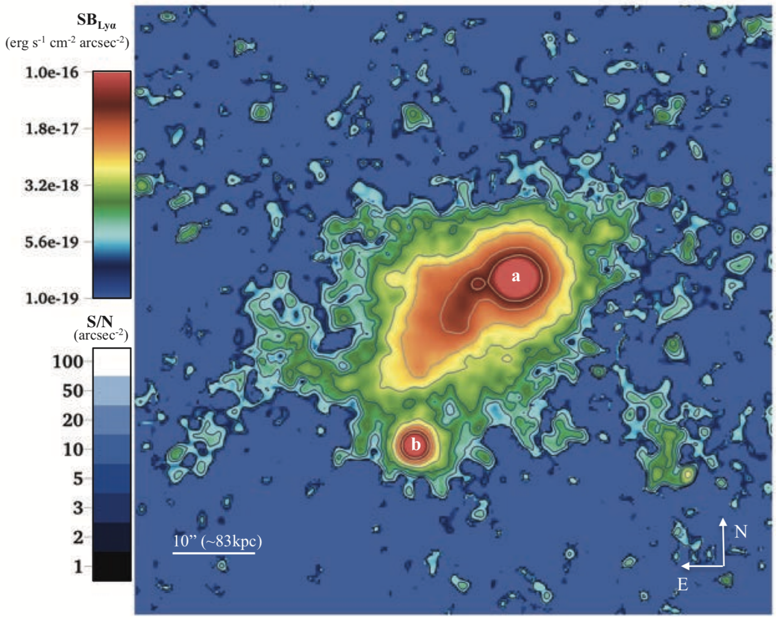

Figure 1.14: Lyman-α image of the UM287 Nebula. From Cantalupo et al. (2014).

which would demand an high resolution and sensitivity, IM consists in the measurement of the spatial fluctuations in the line emission from many galaxies individually not-resolved. This technique is therefore sensitive to all the sources of emission along the line-of-sight. Faint and extended emission sources can be detected easier than with traditional galaxy surveys, although with much poor spatial resolution.

The emission fluctuations is related to the underlying large scale structure of the Universe and the information about the radial distribution along the line-of-sight can be scanned by the frequency dependence. Since large cosmological volumes can be surveyed in a small amount of time, the intensity mapping technique promises to be very efficient for cosmological studies.

This work is based on the 21 cm emission line. However, other emission lines can be studied, especially for astrophysics purposes (see Fig. 1.15):

- The [OIII] line[2] is originated from diffuse and highly ionized regions near young O-type stars: this is an interesting line because may provide informations about low-metallicity environments where photo-dominated regions (PDRs) may occupy only a limited volume of the interstellar medium.

- The [CII] line is instead originated from PDRs at high redshift. It is used to estimate the star formation rate estimates biased by dust extinction, even if it depends strongly on the metallicity. This line can also be used to measure the systemic redshift of the galaxies.

[2]As usual in astrophysics X_n and $[X_n]$ symbols indicate the permitted and forbidden lines of the element X ionized $(n-1)$ times. The roman number $n = I$ therefore indicates a neutral element.

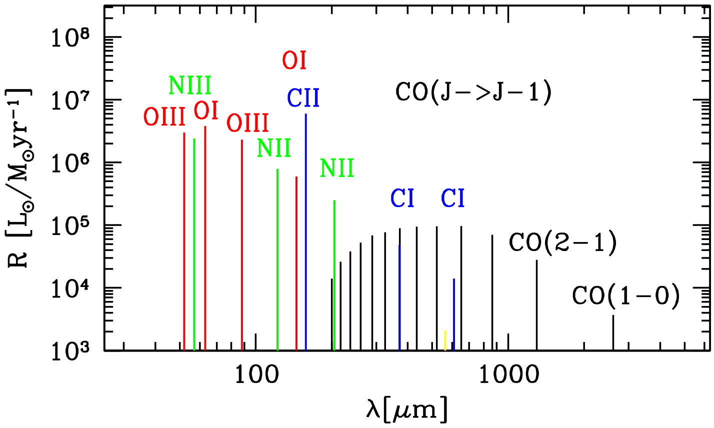

Figure 1.15: Ratio between line luminosity, L, and star formation rate, $\dot{M}_\star$, for various lines observed in galaxies. From Pritchard and Loeb (2012).

- The HeII line, with a frequency of 1640 Å, may be a signature of metal-free Population III stars especially at high-redshifts. It is particularly important because these massive stars produce more HeII ionizing photons than metal enriched stellar populations. Remark however that these stars are formed in small galaxies, very difficult to detect.

- Other lines are typically less luminous.

Many experiments dedicated to several emission lines exist or are upcoming, with an amazing science case spanning from the reionization epoch to star formation, large scale structure and dark energy studies. Table 1.1 lists and Fig. 1.16 illustrates some of the more recent experiments dedicated to IM, showing the redshift range, the angular extent of the survey (upper border of rectangles) and their angular resolution (lower border).

Experiment	Line	Frequency	Redshift range
HERA	HI	50 – 250 MHz	5 – 27
SKA-LOW*	HI	50 – 350 MHz	3 – 27
CHIME*	HI	400 – 800 MHz	0.8 – 2.5
HIRAX*	HI	400 – 800 MHz	0.8 – 2.5
SKA-MID*	HI	350 MHz – 14 GHz	0 – 3
BINGO	HI	939 – 1238 MHz	0.13 – 0.48
LOFAR	HI	115 – 190 MHz	6.5 – 11.4
CCAT-prime	[CII]	185 – 440 GHz	3.3 – 9.3
TIME	[CII]	200 – 300 GHz	5.3 – 8.5
CONCERTO*	[CII]	200 – 360 GHz	4.3 – 8.5
COPSS	CO	27 – 35 GHz	2.3 – 3.3
COMAP	CO	26 – 34 GHz	2.4 – 3.4, 5.8 – 7.8
SPHEREx	Hα, Lyα	60 – 400 THz	0.1 – 5, 5.2 – 8

Table 1.1: Details of some of the ongoing and upcoming intensity mapping experiments.

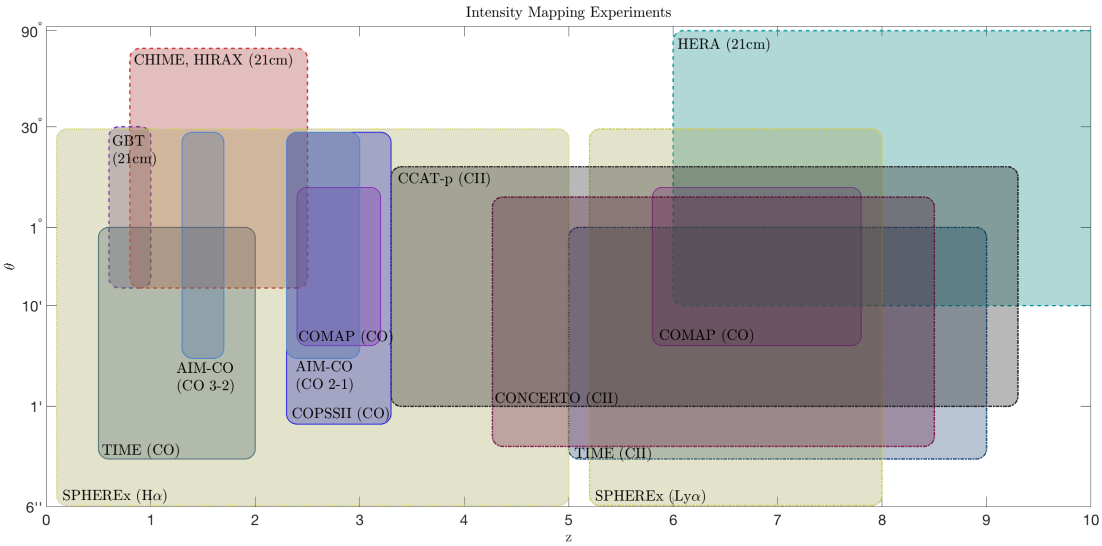

Figure 1.16: A representative list of current and proposed intensity mapping experiments. The redshift range, the maximum resolution and the total sky coverage are reported. From Kovetz et al. (2017).

This thesis considered in particular the SKA project because of the ground breaking results expected from its observations. Once completed, SKA will be able to detect signals from a redshift range $0 < z < 27$, i.e. covering the central part of the reionization epoch. SKA is an international project based on two radio telescopes covering low and mid-range wavebands, under construction in South Africa (SKA-MID) and Australia (SKA-LOW). The first project date back to the 1990s and the first part of the telescope will be completed around 2023 (SKA1, further divided into SKA1-MID and SKA1-LOW). The second part of the project is expected to be completed in late 2020s and it will have a total collecting area of approximately one square kilometre.

The science case covers a very broad list of topics (Taylor, 2013):

- *strong-field tests of gravity*, using pulsars and black holes: pulsars in binary systems with a black hole companions are expected to be detected quite often; in the same way, pulsars can constraint gravity waves physics;
- *origin and evolution of cosmic magnetism*: measurements of polarized synchrotron radiation arising from relativistic particles interacting with magnetic fields will be performed;
- *galaxy evolution and cosmology*: as explained in this Chapter, the 21cm emission line provide informations about cosmic evolution of HI and star formation, allowing also to constraint the equation of state of dark energy;
- *probing the Dark Ages*: the low frequency of the telescope can study the structure of the intergalactic medium before and during the reionization epoch;

- *the cradle of life*: terrestrial planet formation is also an observable of SKA.

During this work, the phase 1 of construction is considered; in particular two instruments will be taken into account, SKA1-MID and SKA1-LOW (Table 1.2).

Experiment	Frequency ν	Resolution	Antennae	Diameter	Area	Location
SKA1-MID	$350\,\mathrm{MHz} - 14\,\mathrm{GHz}$	1 MHz	250	15 m	$0.044\,\mathrm{km}^2$	South Africa
SKA1-LOW	$50 - 350\,\mathrm{MHz}$	1 MHz	911	35 m	$0.88\,\mathrm{km}^2$	Australia

Table 1.2: Technical details of SKA1-MID and SKA1-LOW

Chapter 2

Non-linear evolution of dark matter and neutral hydrogen

2.1 Dark matter simulations

The three-dimensional large-scale structure traced by HI is obtained by Monte Carlo simulations based on dark-matter-only N-body simulations by Carucci et al. (2015), which solve the Newtonian dynamics accounting for either WDM ($m_{\mathrm{WMD}} = 2,\, 3\,\mathrm{keV}$) or CDM in comoving cubic box $L = 100\ h^{-1}$ Mpc. The DM halo catalogues have been extracted by standard FoF techniques with linking length $\mathrm{l} = 0.16$. Catalogues are provided for redshifts $z = 0, 1, 2, 3, 4, 5$.

Using `Pylians` (Villaescusa-Navarro, 2018) and `nbodykit` libraries (Hand et al., 2019), the power spectrum of haloes has been computed. For each catalogue the density field is computed over a grid of 512^3 cells,[1] which correspond to a cell size of length $l = 0.195\ h^{-1}$ Mpc. The mass-assignment scheme used to assign halo masses to the grid is the Cloud-In-Cell one (CIC); given a number density distribution of objects $n(\mathbf{r}) = \sum_j \delta(\mathbf{r} - \mathbf{r}_j)$, where $\mathbf{r}_j$ is the coordinate of the object j, the convolved density value on the $\mathbf{g}$-th grid point $\mathbf{r}_g = \mathbf{g}l$ ($\mathbf{g}$ is an integer vector and l the grid spacing) is

$$n^f(\mathbf{r}_g) = \int n(\mathbf{r}) W(\mathbf{r} - \mathbf{r}_g) \mathrm{d}\mathbf{r}, \tag{2.1}$$

where $W(\mathbf{r})$ is the mass assignment function. In real space for the CIC scheme, the expression of $W(\mathbf{x}) = \Pi_i W(x_i)$ is

$$W(x_i) = \begin{cases} 1 - |x_i|, & |x_i| < 1 \\ 0, & \text{else.} \end{cases} \tag{2.2}$$

Other methods, such as the Nearest Grid Point (NGP) or the Triangular Shaped Cloud (TSC) are often used and the description of these mass assignment schemes in relation with the computation of the power spectrum can be found in Cui et al. (2008).

[1] Indeed a more dense grid would be more appropriate, but considering the dimension of the box the result will not be affected by a different choice.

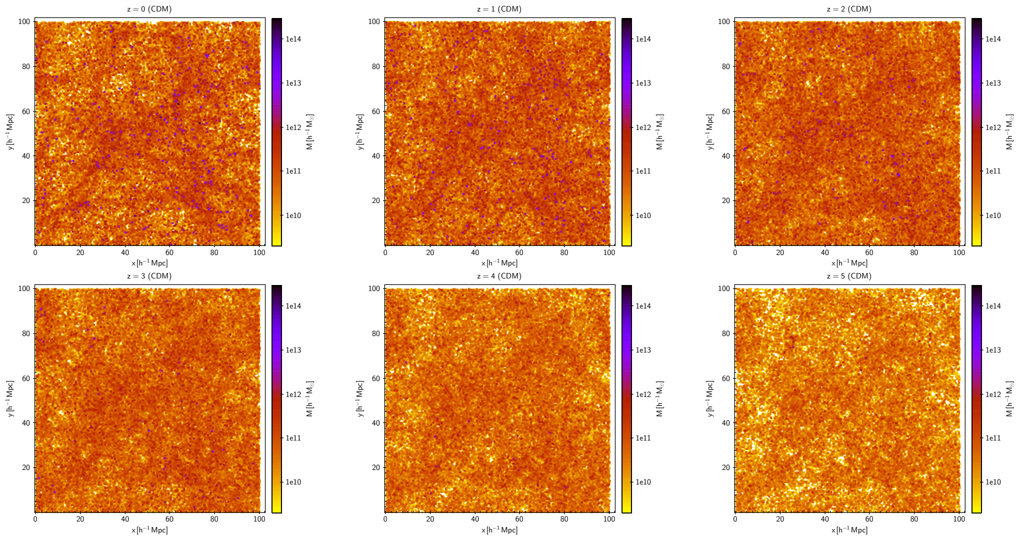

Figure 2.1: 2-dimensional projection of cold dark matter catalogues.

The maximum and minimum comoving wavenumbers are

$$k_{\rm min} = \frac{2\pi}{L/2} \approx 10^{-1}\ h\ {\rm Mpc}^{-1}, \qquad k_{\rm max} = \frac{2\pi}{\bar{d}} \approx 10^{1}\ h\ {\rm Mpc}^{-1}, \tag{2.3}$$

where $\bar{d}$ is the mean distance between halos, defined by $\frac{4\pi}{3} N_h \bar{d}^3 = L^3$.

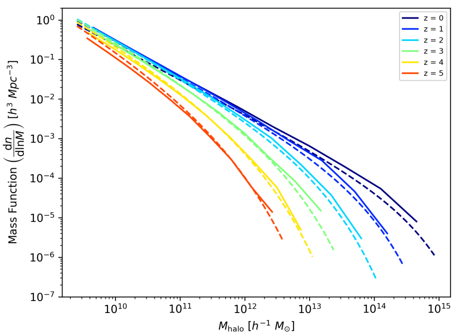

Figure 2.2: Halo cold dark matter mass function (*solid*), compared to the Sheth-Tormen one (*dashed*).

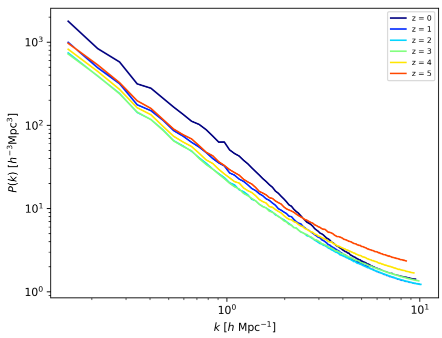

Figure 2.3: Power spectrum computed from catalogues with $z \in [0, 5]$.

Cold dark matter. The number and mass range of CDM haloes are reported in Table 2.1 as function of redshift. As shown in Fig. 2.1, the filamentary structure on large scales becomes progressively more evident at late time. The halo mass function is reported in Fig. 2.2, compared to the Sheth-Tormen mass function. There is a good agreement

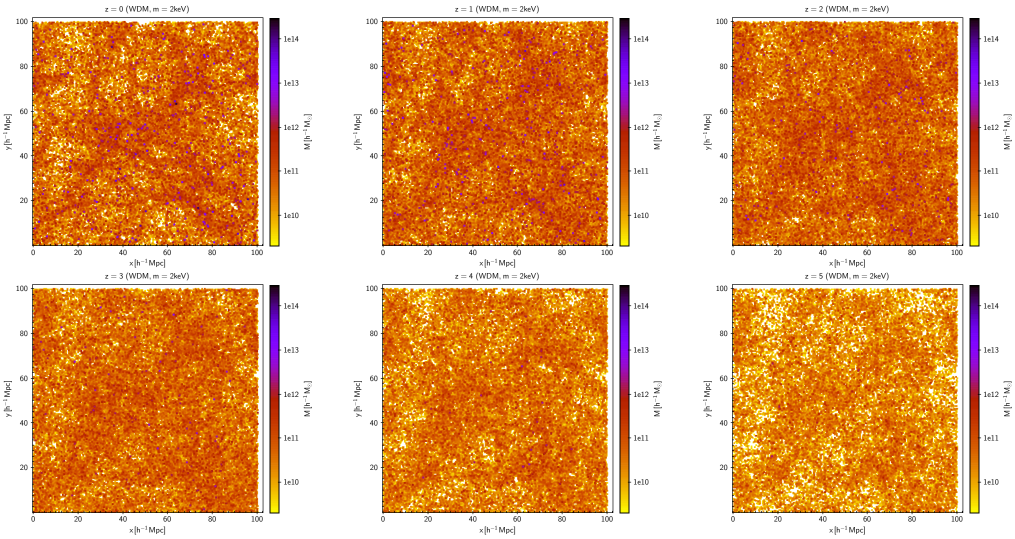

Figure 2.4: Warm dark matter haloes evolution for $m_{\mathrm{WDM}} = 2\,\mathrm{keV}$. For $m_{\mathrm{WDM}} = 3\,\mathrm{keV}$ there is no visible difference and it is not shown.

between the two. Finally, the power spectrum is shown in Fig. 2.3: to be noted the asymptotic trend for larger k and small scales, tracing instead the evolution on large scales.

z	0	1	2	3	4	5
N_{haloes}	$834,092$	$975,122$	$1,011,773$	$944,381$	$793,404$	$599,559$
$M_{\mathrm{min}}\,[h^{-1}\,\mathrm{M}_{\odot}]$			$2.6 \cdot 10^{9}$			
$M_{\mathrm{max}}\,[h^{-1}\,\mathrm{M}_{\odot}]$	$8.5 \cdot 10^{14}$	$2.8 \cdot 10^{14}$	$1.1 \cdot 10^{14}$	$2.4 \cdot 10^{13}$	$1.1 \cdot 10^{12}$	$3.8 \cdot 10^{11}$

Table 2.1: Number of haloes and maximum and minimum masses per catalogue.

Warm dark matter. WDM halo catalogues were provided with two WDM masses, $m_{\mathrm{WDM}} = 2\,\mathrm{keV}$ and $3\,\mathrm{keV}$. Like for CDM the number of haloes and the maximum and minimum masses are reported in Table 2.2. As expected, the number of haloes with warm

m_{WDM}	z	0	1	2	3	4	5
	N_{haloes}	$653,284$	$756,190$	$776,214$	$709,688$	$583,553$	$433,809$
2 keV	$M_{\mathrm{min}}\,[h^{-1}\,\mathrm{M}_{\odot}]$				$2.6 \cdot 10^{9}$		
	$M_{\mathrm{max}}\,[h^{-1}\,\mathrm{M}_{\odot}]$	$8.5 \cdot 10^{14}$	$2.8 \cdot 10^{14}$	$1.1 \cdot 10^{14}$	$2.3 \cdot 10^{13}$	$1.1 \cdot 10^{13}$	$3.7 \cdot 10^{12}$
	N_{haloes}	$746,236$	$872,016$	$902,648$	$837,065$	$696,366$	$521,722$
3 keV	$M_{\mathrm{min}}\,[h^{-1}\,\mathrm{M}_{\odot}]$				$2.6 \cdot 10^{9}$		
	$M_{\mathrm{max}}\,[h^{-1}\,\mathrm{M}_{\odot}]$	$8.5 \cdot 10^{14}$	$2.8 \cdot 10^{14}$	$1.1 \cdot 10^{14}$	$2.3 \cdot 10^{13}$	$1.1 \cdot 10^{13}$	$3.7 \cdot 10^{12}$

Table 2.2: Number of haloes per catalogue.

dark matter is systematically lower than the ones for cold dark matter: less massive and therefore faster particles (see the free-streaming wavelength described in Chapter 1), that slows the formation of structures on large scales. The halo mass function is reported in Fig. 2.5 for both masses. Again it is in well agreement with the Sheth-Tormen mass function, even if the measured one is systematically lower for small masses. Finally, the power spectrum is shown in Fig. 2.6 for both masses.

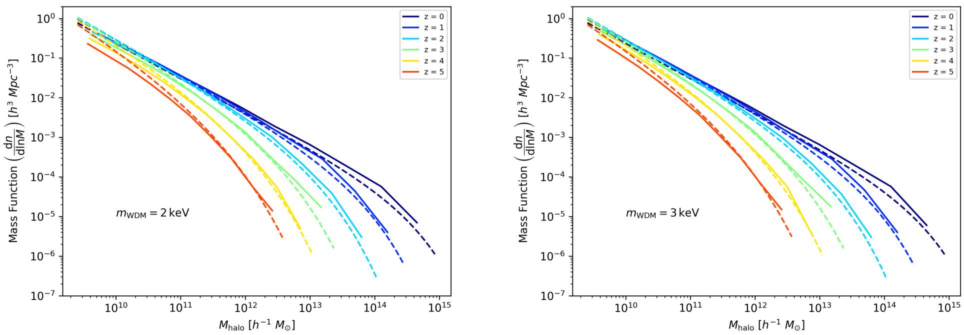

Figure 2.5: Halo warm dark matter mass function (*solid line*), compared to the Sheth-Tormen one (*dashed line*). On the *left* for $m_{\rm WDM} = 2\,\rm keV$ and on the *right* for $m_{\rm WDM} = 3\,\rm keV$.

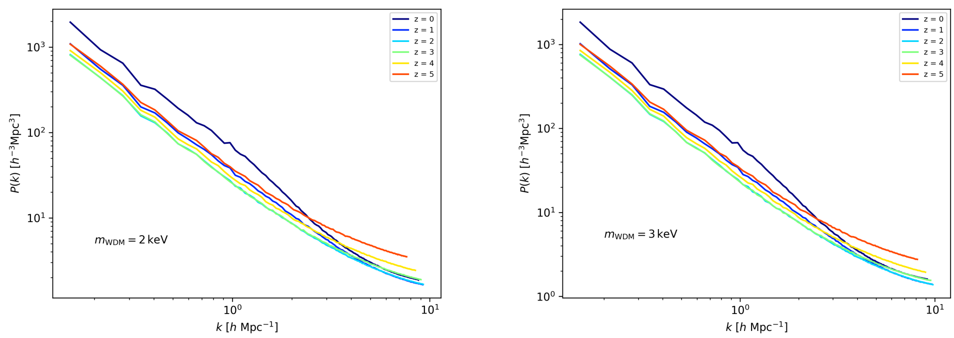

Figure 2.6: Power spectrum computed from catalogues with $z \in [0, 5]$. On the *left* for $m_{\rm WDM} = 2\,\rm keV$ and on the *right* for $m_{\rm WDM} = 3\,\rm keV$.

Important differences in CDM and WDM structures are clear. As shown in Fig. 2.7, while for halo masses larger than $\backsim 10^{11}\,h^{-1}\,M_\odot$ the difference between the two cosmologies are not evident, as dominated by sample variance, for masses lower than $\backsim 10^{11}\,h^{-1}\,M_\odot$ the mass function for lighter dark matter particles is smaller by 20-25 percent: the number count of dwarf galaxies is a clear probe for the nature of the DM candidate.

The power spectrum is shown in Fig. 2.8: the lighter is the dark matter particle and the larger values the power spectrum assumes, because of the less power of the signal caused by the free-streaming length.

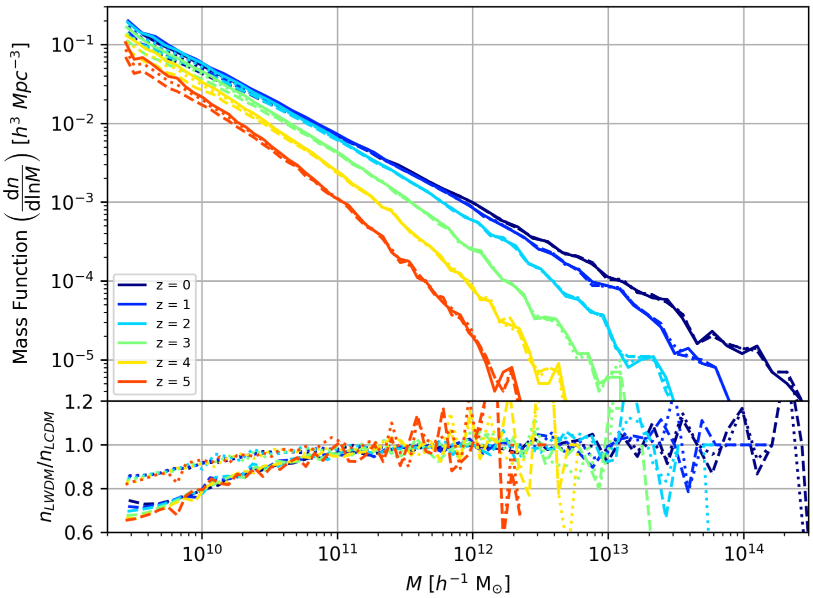

Figure 2.7: Halo mass function for cold dark matter (*solid line*), warm dark matter with $m_{\mathrm{WDM}} = 2\,\mathrm{keV}$ (*dashed line*) and warm dark matter with $m_{\mathrm{WDM}} = 3\,\mathrm{keV}$ (*dotted line*).

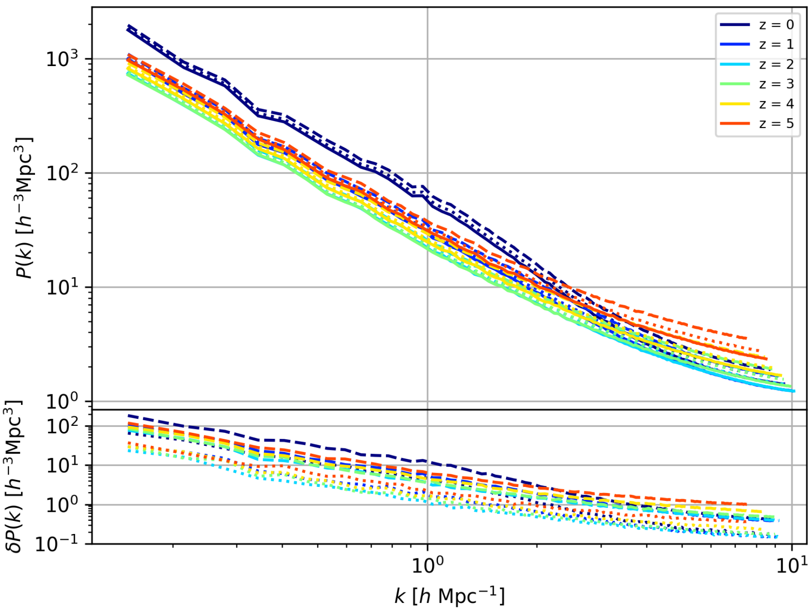

Figure 2.8: Power spectrum for cold dark matter (*solid line*), warm dark matter with $m_{\mathrm{WDM}} = 2\,\mathrm{keV}$ (*dashed line*) and warm dark matter with $m_{\mathrm{WDM}} = 3\,\mathrm{keV}$ (*dotted line*).

2.2 Halo HI mass

Villaescusa-Navarro, Genel, et al. (2018) proved that neutral hydrogen essentially collapse within dark matter haloes and that the amount of neutral hydrogen outside the dark matter haloes is negligible. From virialisation arguments, Bagla, Khandai, and Datta (2010) shown that the maximum and minimum masses, $M_{\max}$ and $M_{\min}$ are related to the dark matter halo circular velocity $v_{\rm circ}$ through

$$M = 10^{10} M_{\odot} \left(\frac{v_{\rm circ}}{60\,{\rm km\,s^{-1}}} \right)^3 \left(\frac{1+z}{4} \right)^{-3/2} , \tag{2.4}$$

$M_{\max}$ is obtained for $v_{\rm circ} \simeq 200\,{\rm km\,s^{-1}}$, $M_{\min}$ for $v_{\rm circ} \simeq 30\,{\rm km\,s^{-1}}$. A fast approach is to use Halo Occupation Distribution (HOD) techniques, where the HI content of dark matter haloes depends only on halo mass, defining the *HI halo mass* $M_{\rm HI}(M)$. Although, it does not model the spatial distribution of HI within dark matter haloes and it neglect possible environmental dependencies. Another approach is to model the HI distribution taking into account the cosmological context with hydro-dynamical simulations (Villaescusa-Navarro, Genel, et al., 2018): in these simulations the physical processes included are the star formation, the feedback from stellar winds, supernovae and Active Galactic Nuclei (AGN) and black hole accretion. Different empirical models for the HI halo mass $M_{\rm HI}(M)$ have been proposed (e.g. Bagla, Khandai, and Datta (2010), Villaescusa-Navarro, Genel, et al. (2018), Baugh et al. (2019)). The expectation is a linear relation between halo DM mass and HI mass, above a certain mass threshold, since low mass haloes are not expected to host large amounts of HI (due to astrophysics processes like tidal stripping and photo-ionization). The more recent and complete model is the one proposed in Spinelli et al. (2019) and it is the one used here the semi-empirical form fitted on hydro-dynamical simulations is

$$M_{\rm HI}(M) = M \left[a_1 \left(\frac{M}{10^{10}} \right)^{\beta} e^{-\left(\frac{M}{M_{\rm break}} \right)^{\alpha}} + a_2 \right] e^{-\left(\frac{M_{\min}}{M} \right)^{0.5}} ; \tag{2.5}$$

see Table 2.3 for the values of parameters. At low-mass the relation is asymptotically

z	a_1	a_2	α	β	$\log_{10}(M_{\rm break})$ $(h^{-1}\ {\rm M}_{\odot})$	$\log_{10}(M_{\min})$ $(h^{-1}\ {\rm M}_{\odot})$
0	0.42	$8.7 \cdot 10^{-4}$	$-3.7 \cdot 10^{-5}$	-0.70	12.1	11.4
1	$3.8 \cdot 10^{-3}$	$1.6 \cdot 10^{-3}$	0.24	1.70	8.30	-1.3
2	$5.8 \cdot 10^{-4}$	$1.5 \cdot 10^{-3}$	0.52	0.63	11.66	-3.11
3	$1.7 \cdot 10^{-3}$	$4.4 \cdot 10^{-4}$	0.47	0.23	12.30	-2.23
4	$1.7 \cdot 10^{-3}$	$3.4 \cdot 10^{-4}$	0.55	0.19	12.26	-2.75
5	$5.2 \cdot 10^{-3}$	$-5.5 \cdot 10^{-4}$	0.05	0.04	12.20	-3.71

Table 2.3: Coefficients for HI mass (2.5).

scale-free ($M_{\rm HI} \propto M^{\beta}$), with a tiny though not vanishing offset (a_2). The exponential cut-off accounts for the absence of HI in high-mass haloes, because of tidal stripping and photo-ionization ($T_{\mathrm{vir}} \sim 10^4$ K for $M_{\mathrm{vir}} \sim 10^{14}\, h^{-1}\, M_{\odot}$). Equation (2.5) fits the results from hydrogen simulations at several redshifts illustrating the stochastic relation between M_h and M_{HI}; see Fig. 2.9.

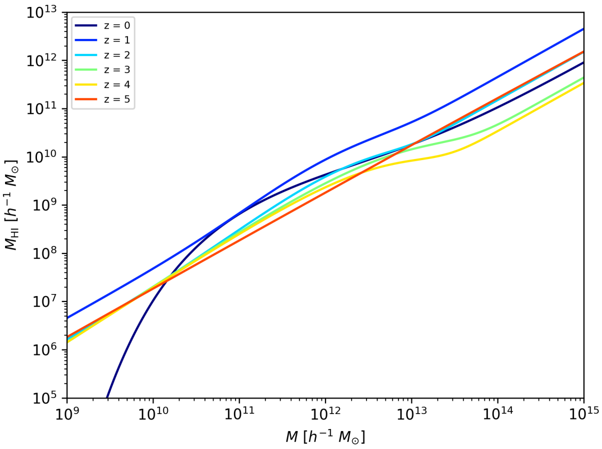

Figure 2.9: HI halo mass for different redshift, according to equation (2.5) and to Table 2.3.

To quantify the scatter of the $M_{\mathrm{HI}}(M)$, in Fig. 2.10 the density distribution of the HI mass hosted by haloes of different mass, at different redshifts, is shown (Spinelli et al., 2019). In red, the semi-analytical model in equation (2.5).

The neutral hydrogen density is defined as

$$\Omega_{\mathrm{HI}}(z) = \frac{\rho_{\mathrm{HI}}(z)}{\rho_{c,0}}, \tag{2.6}$$

and it is approximately constant with redshift, assuming a value of $\Omega_{\mathrm{HI}} \approx 10^{-3}$. In Fig. 2.11, the abundance of neutral hydrogen from several observational sources is shown.

Several attempts have been made to fit the observations taking into account many of the physical processes involved. One can obtain the mean HI density parameter averaging the HI mass relation $M_{\mathrm{HI}}(M)$ over the halo mass function distribution $n(M)$, i.e.

$$\Omega_{\mathrm{HI}}(z) = \frac{1}{\rho_{c,0}} \int_0^{\infty} n(M,z) M_{\mathrm{HI}}(M,z) \mathrm{d}M, \tag{2.7}$$

At higher redshift, the model predicts a clear decrease of $\rho_{\mathrm{HI}}(z)$ with respect to the observational data (bottom of Fig. 2.11). This trend is shared by independent semi-analytic models (e.g. Lagos et al. (2014)), while hydro-dynamical simulations generally predict an opposite trend or significantly weaker evolution (e.g. Villaescusa-Navarro, Genel, et al. (2018)). At high redshift, the observational measurements are based on Damped Lyman-α systems (DLα): although the physical origin of these systems is still debated, the measurements based on these objects are robust.

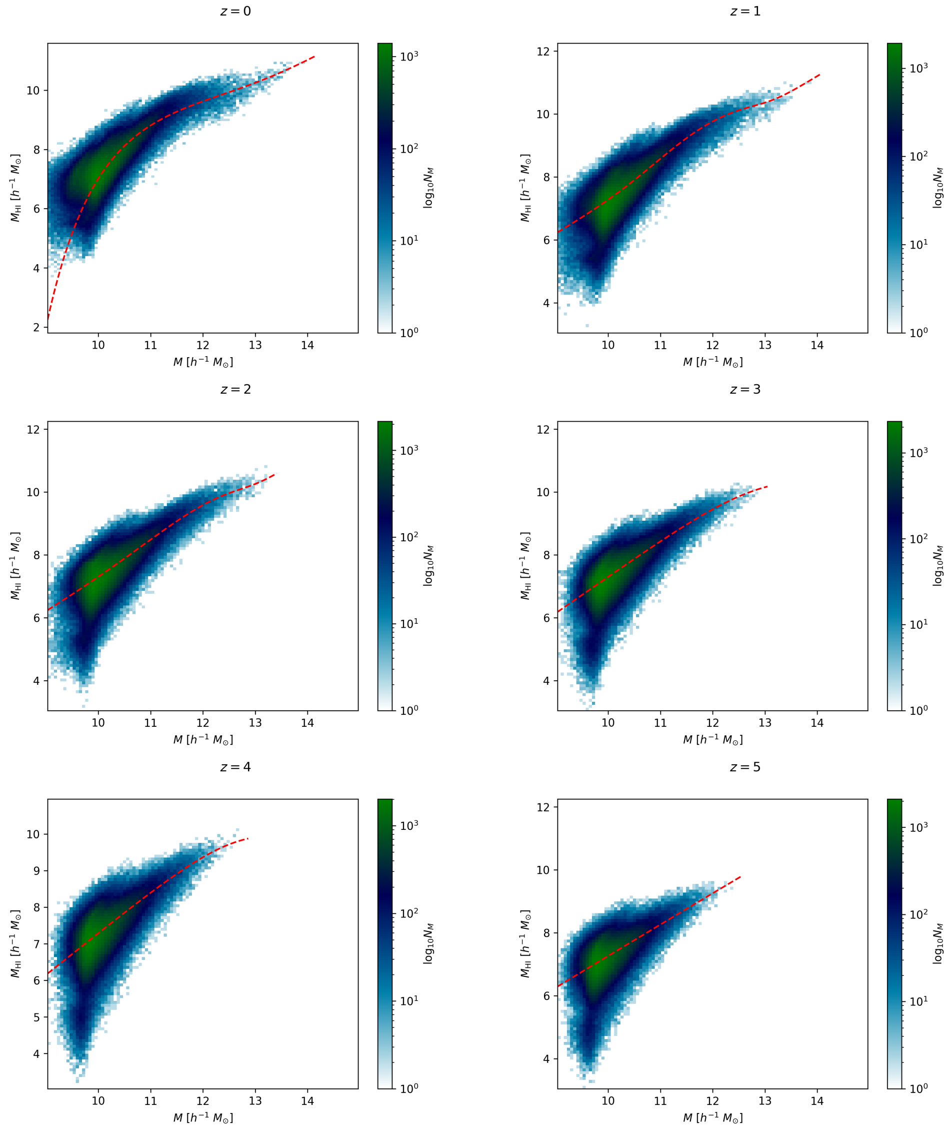

Figure 2.10: Scatter of $M_{\rm HI}(M)$ from hydrodynamical simulations. In red the fit of equation (2.5). From Spinelli et al. (2019).

According to Villaescusa-Navarro, Genel, et al. (2018), the HI bias function $b_{\rm HI}(z)$ can be obtained by the halo mass function $n(M,z)$ (equation (1.84)), the halo HI mass $M_{\rm HI}(M)$ (equation (2.5)) and the bias $b(M)$ (equation (1.85)) as

$$\begin{aligned} b_{\rm HI}(z) &= \frac{1}{\rho_{c,0}\Omega_{\rm HI}(z)} \int_0^\infty n(M,z) b(M,z) M_{\rm HI}(M,z) \mathrm{d}M = \\ &= \frac{\int_0^\infty n(M,z) b(M,z) M_{\rm HI}(M,z)\, \mathrm{d}M}{\int_0^\infty n(M,z) M_{\rm HI}(M,z)\, \mathrm{d}M}. \end{aligned} \tag{2.8}$$

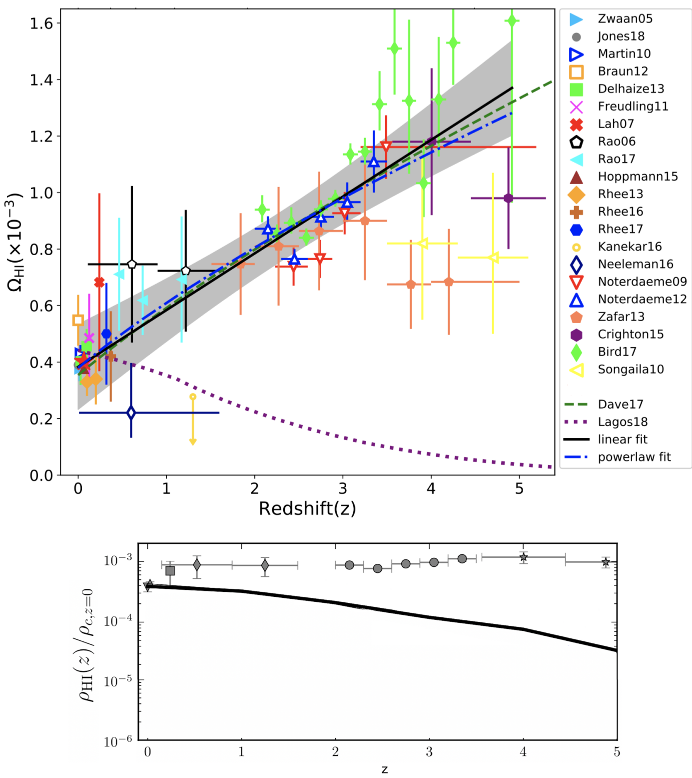

Figure 2.11: (*Top*) cosmic HI density Ω_{HI} measurements plotted as a function of redshift from different sources. The linear weighted fit of all Ω_{HI} measurements and its 95% confidence interval is shown as a black line with grey area. The blue dash-dot line shows the powerlaw fit of all measurements. From Hu et al. (2019). (*Bottom*)the trend of $M_{\text{HI}}(M)$ described in equation (2.5) with respect to the observations. A clearly descreasing evolution with redshift is shown. From Spinelli et al. (2019).

Remark that the $M_{\text{HI}}(M)$ proposed in this work is valid in the range of halo masses probed by the simulations, so $2 \times 10^9\, h^{-1}\text{M}_\odot < M < 10^{15}\, h^{-1}\text{M}_\odot$. The integration boundaries in equation (2.8) are fixed according.

The halo bias $b(M)$ is computed as follows. Firstly the mass variance $\sigma(M)$ was computed according to equation (1.64) using the linear matter spectrum computed with `CAMB` (for CDM) and eventually corrected (for WDM, see equation (1.58)). Sheth Mo Tormen bias $b(M)$ (equation (1.85)) is then obtained using the ΛCDM value for δ_c. It is shown in Fig. 2.13. The bias computed are reported in Table 2.4, along with the HI density, computed according to equation (2.7). There is not a clear difference between the bias computed for CDM and WDM particles: one can notice that in general the lower is the dark matter mass and the higher is the bias at high redshift, but the differences are less than 1 percent and therefore the three models can not be distinguished. The two CDM quantities are compared with the ones computed in Villaescusa-Navarro, Genel, et al. (2018): here the bias is calculated as

$$b_{\mathrm{HI}}(k) = \sqrt{\frac{P_{\mathrm{HI}}(k)}{P_{\mathrm{m}}(k)}}. \tag{2.9}$$

The values on large scales (small k) should be equal to the linear HI bias computed above; small corrections are interpreted as box-size effect. This assumption is in agreements with the results of Anderson et al. (2018) and Springel et al. (2018).

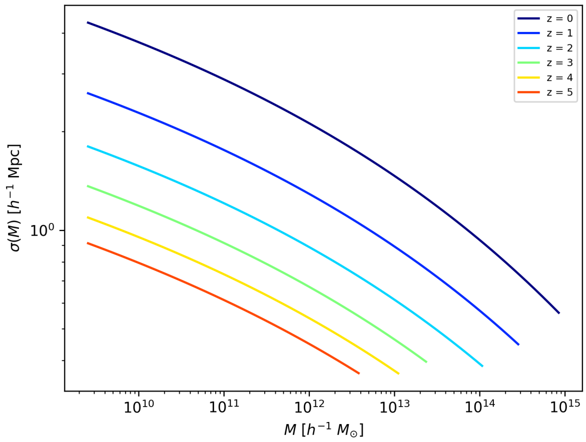

Figure 2.12: Mass variance computed for redshifts $0 \leq z \leq 5$, depending on the mass, in ΛCDM cosmology. The differences with the ones for a ΛWDM cosmology are not visible and so the corresponding figures are not reported.

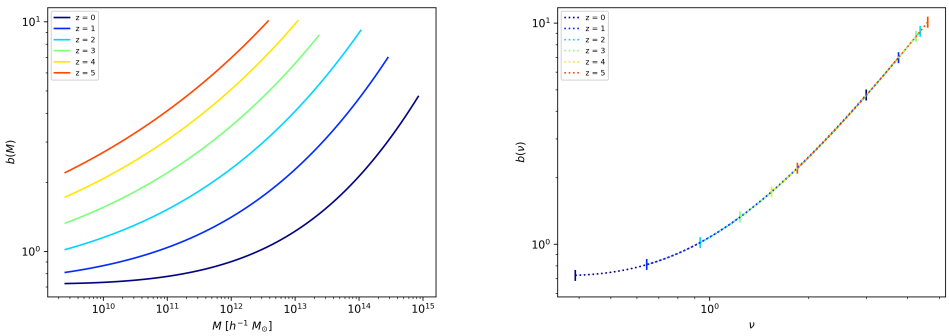

Figure 2.13: Dark matter bias computed for redshifts $0 \leq z \leq 5$, depending on the mass M (*left*) and on ν (*right*), according to the Sheth, Mo, Tormen (2001) model, for a ΛWDM cosmology.

m_{WDM}	z	0	1	2	3	4	5
$\gg$ keV (CDM)	b_{HI}	1.03	1.45	1.89	2.31	2.77	3.21
	$\Omega_{\text{HI}} \cdot 10^3$	0.43	0.41	0.23	0.13	0.07	0.04
	$b_{\text{HI}}^{\text{th}}$	0.84	1.49	2.03	2.56	2.82	3.18
	$\Omega_{\text{HI}}^{\text{th}} \cdot 10^3$	1					
2 keV	b_{HI}	1.04	1.46	1.90	2.33	2.81	3.28
	$\Omega_{\text{HI}} \cdot 10^3$	0.43	0.41	0.23	0.13	0.07	0.04
3 keV	$b_{\text{HI}}^{\text{th}}$	1.04	1.45	1.90	2.32	2.79	3.24
	$\Omega_{\text{HI}} \cdot 10^3$	0.43	0.41	0.23	0.13	0.07	0.04

Table 2.4: Bias b_{HI} and Ω_{HI} computed for WDM scenario.

2.3 HI Monte Carlo simulations

Monte Carlo sampling techniques are applied to the dark matter catalogues, to obtain a synthetic HI catalogue. These simulations are performed with two methods: a parametric model and a non-parametric model. Remark the one-to-one correspondence between DM and HI haloes. For each catalogue, 100 realization of HI distribution have been simulated.

Parametric model. Given a dark matter halo of mass M_{h}, a Gaussian probability density function $\mathcal{N}(\mu_{\text{HI}}, \sigma^2_{\text{HI}})$ is defined with mean $\mu = M_{\text{HI}}(M_{\text{h}})$ given by equation (2.5) and variance $\sigma^2_{\text{HI}} = b^2_{\text{HI}}\sigma^2(M_{\text{h}})$ given by equations (2.8) and (1.64). The final HI catalogue is obtained by the standard inverse transform sampling method.

Non-parametric model. Instead of inversion sampling, a Monte Carlo sampling can be performed directly from the mass relation measured in HI-DM hydro-dynamical simulations, interpreted as two-dimensional probability distribution function $p(M_h, M_{\text{HI}})$. Given a dark matter halo of mass M_{h}, the corresponding conditional pdf $p_{\text{HI}}(M_{\text{HI}}|M_h)$ of Fig. 2.10 is used for a new inverse transform. the procedure is illustrated in Fig. 2.14 for redshift $z = 4$.

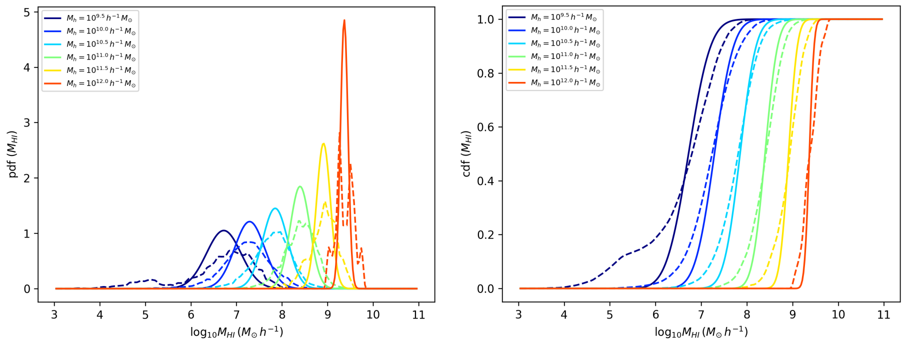

Figure 2.14: Conditional pdf (*left*) and cdf (*right*) of M_{HI}, for fixed dark matter mass M_h. Continuous line for the parametric model and dashed for the non-parametric one.

Compared to the (Gaussian) sampling based on the parametric model of $M_{\mathrm{HI}}(M)$,

1. it is no more necessary to use a semi-analytical model such as the one in equation (2.5), whose expression can not reproduce correctly the amount of neutral hydrogen in the Universe at high redshifts,

2. in the semi-analytical model a cut-off for small dark matter masses is present according to (2.4), but there is not indication on the dark matter halo maximum mass to host a neutral hydrogen distribution; with the non-parametric model, the probability of obtaining an HI halo for large DM masses is intrinsically vanishing,

3. for DM haloes with intermediate masses, the HI mass is strictly related to the physics of the processes accounted for by the simulation, which is in general more reliable.

Chapter 3

21 cm Intensity Mapping

3.1 Temperature maps: algorithm

The three-dimensional HI realizations simulated in Chapter 2 are used to create two-dimensional maps of temperature, as follows:

1. The HI density field is resampled on a Cartesian grid of 1024^3 cells using the CIC mass assignment scheme already described in Chapter 2. A finer grid e.g. of 2048^3 cells as in Villaescusa-Navarro, Genel, et al. (2018), whose cells are comparable to the virialization radius of an HI halo, would be more appropriate but computationally expensive for this preliminary work.

2. In order to observe the radiation emitted at redshift z a slice of the HI density field with comoving width d is selected to reproduce the appropriate frequency bandwidth. For the SKA-1 survey, with frequency resolution is $\delta f = 1$ MHz the relation $f(z) = f_0/(1+z)$ between the observed and rest-frame frequencies f and f_0 yields the limits of the redshift range

$$z - \delta z_{\mathrm{i}} = \frac{f_0}{f(z) + \delta f/2} - 1, \qquad z + \delta z_{\mathrm{f}} = \frac{f_0}{f(z) - \delta f/2} - 1, \tag{3.1}$$

corresponding to a comoving width

$$d = \chi(z + \delta z_{\mathrm{f}}) - \chi(z - \delta z_{\mathrm{i}}) = \int_{z-\delta z_{\mathrm{i}}}^{z+\delta z_{\mathrm{f}}} c\frac{\mathrm{d}z}{H(z)}, \tag{3.2}$$

where $\chi(z)$ is the comoving radial distance. The HI mass densities $\rho_{\mathrm{HI}}(\mathbf{x})$ are obtained dividing each three-dimensional cell by the volume of the cell itself.

3. The slice is then projected onto a two-dimensional grid. A weight is associated to each grid points along the line-of-sight. One can choose, for example, to assign a larger weight to closer points on the line-of-sight, taking into account the spectral resolution.

4. The HI densities are transformed to brightness temperature through equation (1.97), written in a more convenient way as

$$\delta T_b(\mathbf{x}) = 189h\frac{H_0}{H(z)}(1+z)^2\frac{\rho_{\rm HI}(\mathbf{x})}{\rho_c}\,\mathrm{mK}. \tag{3.3}$$

5. To account for the angular resolution, the two-dimensional grid is convolved with a Gaussian filter of rms-variance

$$\sigma_\theta(z) = \frac{\theta\,\chi(z)}{2\sqrt{2\ln 2}}, \tag{3.4}$$

where θ is the desired angular resolution. For intensity mapping studies, Bull et al. (2015) showed that the best approach is via single-dish observations, for which the angular resolution is given by

$$\theta = \frac{\lambda(z)}{D} = \frac{\lambda_0(1+z)}{D}, \tag{3.5}$$

with D the diameter. For the single dish for SKA experiments is reported in Table 1.2, according to redshift: for $z = 1$, 2 SKA-MID is considered ($D = 15$m), for $z = 3$, 4, 5 SKA-LOW is considered ($D = 35$m). Table 3.1 summarizes the parameters for $1 \leq z \leq 5$. The procedure is completely general and can therefore be applied also to other intensity line surveys.

z	f (MHz)	$d\,(h^{-1}\,\mathrm{Mpc})$	$N_{\rm slices}$	$\sigma_\theta\,(h^{-1}\,\mathrm{Mpc})$
1	710.0	4.75	21	27.51
2	473.3	6.30	15	64.56
3	355.0	7.45	13	45.22
4	284.0	8.38	11	63.73
5	236.7	9.21	10	82.90

Table 3.1: Parameters used to create maps of temperature, according to equations (3.2) and (3.4).

For larger redshifts, the slice width necessary to obtain the desired frequency resolution increases: an higher number of HI haloes are therefore needed to attain the same level of accuracy. Large value of the Gaussian filter variance lowers the resolution of the maps, being comparable to the box-size. Catalogues at redshift $z = 0$ were not considered, since the projection is geometrically meaningless.

3.2 Intensity maps

The intensity maps in ΛCDM and ΛWDM cosmologies at $z = 1$, 2, 3, 4, 5 i.e. the relative temperature fluctuations $(\delta T_b - \overline{\delta T}_b)/\sigma_{\delta T_b}$ are shown in Fig. 3.1.

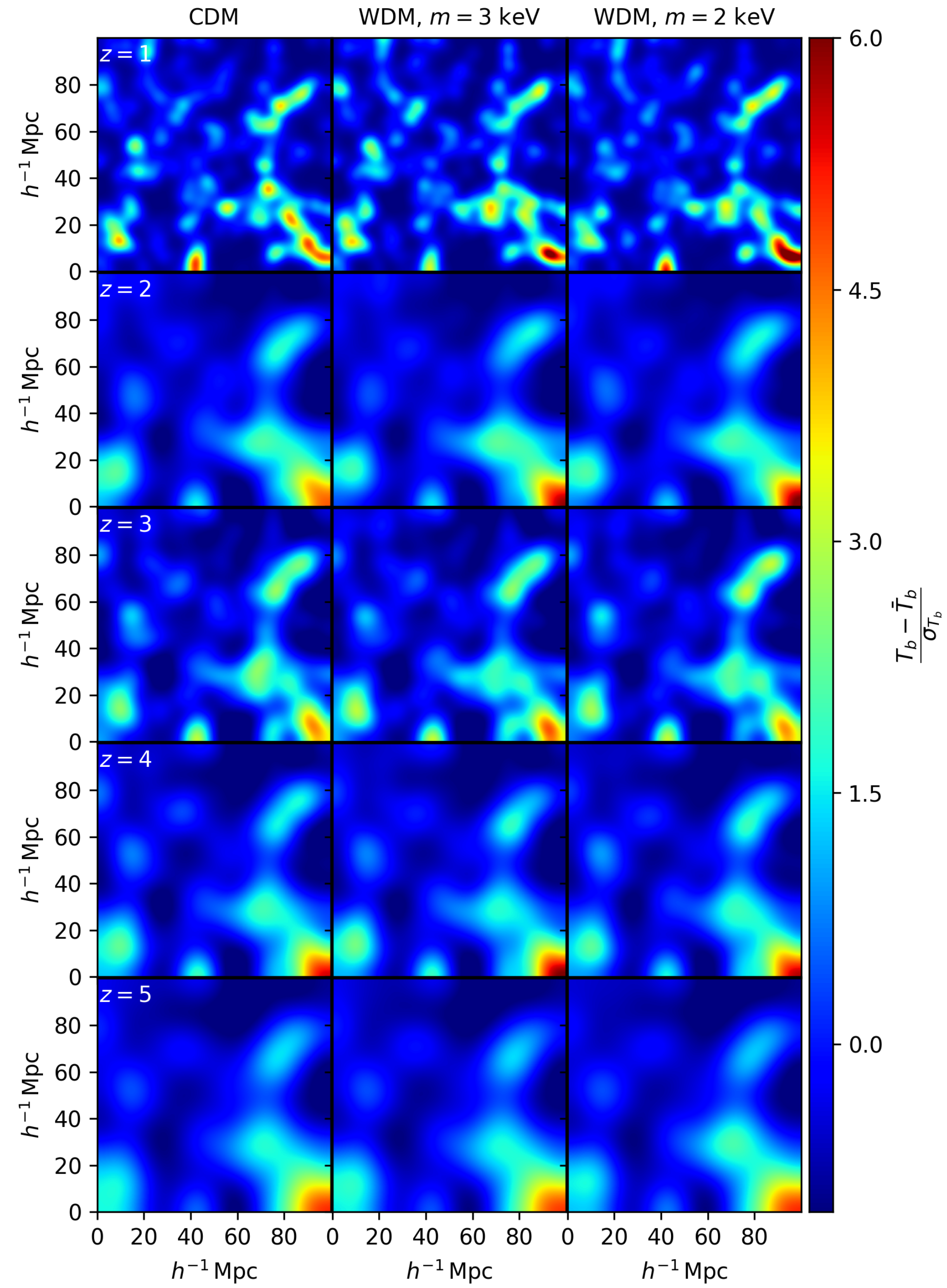

Figure 3.1: Maps of intensities for redshifts (from top to bottom) $1 \leq z \leq 5$ of the same slice.

The resolution is progressively decreasing at higher redshifts. A remarkable exception is the map at $z = 3$, due to the change of parameters from SKA-MID to SKA-LOW: being the rms-variance (3.4) proportional to D^{-1}, at $z = 3$ SKA-LOW parameters are used and therefore the resolution is improved. Nevertheless, even if only one realization of HI distribution is considered here, some difference is already visible in the three models at $z = 1$. Large-scale structure traced by HI becomes more sharpened at lower redshifts, reflecting the evolution of the underlying filamentary structure discussed in Chapter 2. It is worth noticing that the values of temperature fluctuations are for the most part positive, i.e. $\delta T_b > \overline{\delta T_b}$, meaning that the hydrogen line is in emission and not in absorption according to equation (1.97) and to the post-reionization phase, which occurs in the redshift range $0 \lesssim z \lesssim 5$.

For each redshifts, five not-adjacent slices have been considered in order to avoid a cross-correlated signal. For each slice, only 50 maps of intensities have been computed, due to the high computational costs required by the map-making algorithm.

Chapter 4

Minkowski Functionals analysis

4.1 Definition

A mathematically well-established technique to quantify the morphology of the large-scale structure, completing the information obtained using cumulants and correlation functions, is based on the Minkowski functionals (MFs) $V_k^{(d)}$, integral measures which generalise the notion of volume accounting for the content, shape (geometry) and connectivity (topology) of spatial patterns. In two dimensions, the MFs of a continuous body correspond to its surface area V_0, perimeter V_1, and the Euler characteristic V_2 which accounts of the number of isolated regions minus the number of holes. MFs were first introduced in cosmology by Mecke, Buchert, and Wagner (1994), generalizing the seminal study by Gott, Melott, and Dickinson (1986) on the topology of the large-scale structure based on the genus curve. The power of MFs originates in the characterisation theorem Hadwiger (1957), which proves that for any convex sets in d dimensions and, as an extensions, for the convex ring of all unite unions of convex bodies, there exist only $d + 1$ linearly independent measures (the MFs) that preserve additivity, motion invariance under Galilean transformations, and conditional continuity under the Hausdorff measure. These properties

1. assure that these global functionals can be obtained by summing up their local contributions, with a consequent computational effort always of order $O(N)$ for N sources, unlike n-point correlation functions for which it is $O(N \log N)$ for $n = 2$ and $O(Nn)$ for $n \geq 3$;

2. support the principal kinematical formula, which provides an explicit prescription to deal with irregular boundaries of the survey;

3. guarantee convergence when dealing with iterative smoothing, the result being robust against short-scale spatial irregularities.

It is worth to stress the importance of the whole set of MFs and so of the study of the morphology of structures. For illustration, let us consider the patterns in Fig. 4.1a and 4.1b: both figures have the same number of objects (3 simply connected sets) and they

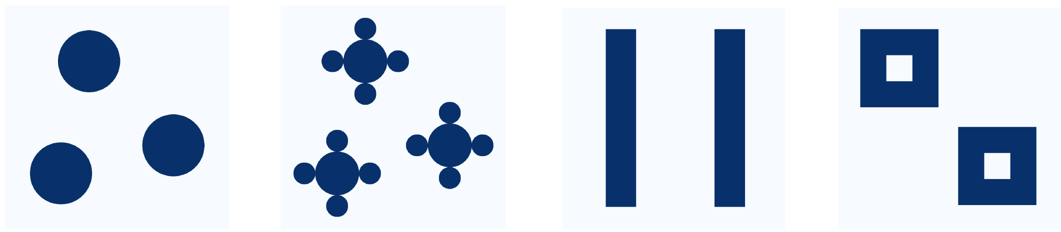

(a) (b) (c) (d)

Figure 4.1: A representation of a two-dimensional distribution. Figures 4.1a and 4.1b share the same number of isolated regions and holes and the same area, but not the same perimeter. Vice versa, Figures 4.1c and 4.1d have the same area and perimeter, but a different Euler characteristic.

have been constructed with the same area A. Namely, the MFs V_0 (area) and V_2 (Euler characteristic) will not be able to distinguish the two figures. Conversely, V_1 (perimeter) is different in the two cases. Saying R' the radius of the three identical disks in Fig. 4.1a, and R (r) the radius of the inner (outer) disks in Fig. 4.1b (let us consider $n = 3$ inner disks and $N = 4$ outer disks), the equivalence of the surface areas of the two sets reads

$$n\pi R'^2 = n\pi R^2 + nN\pi r^2, \tag{4.1}$$

giving $R' = \sqrt{R^2 + Nr^2}$, the condition to obtain the same perimeter is

$$2\pi R' = 2\pi R + 2N\pi r = 2\pi\sqrt{R^2 + Nr^2}, \tag{4.2}$$

which reads

$$R = \frac{1-N}{2}r, \tag{4.3}$$

which has no positive solution for $N > 1$. Vice versa, different objects with the same perimeter will be distinguish from the area. The Euler characteristic gives information about the number of the objects: consider the shapes in Fig. 4.1c and 4.1d, where all the objects have been generated with the same area and perimeter. In this case, the Euler characteristic (which is equal to the number of objects over a given threshold minus the number of objects under the threshold), will be different for each frame and therefore V_2 can distinguish between the two.

Being the 21 cm IM highly non-Gaussian, MFs are well suited for their analysis. Remark that MFs contain implicitly information about higher order moments (n-point correlation functions), which enables one to draw conclusions about the statistical spatial properties of patterns not accessible by two-point statistics (the power spectrum informs only about the amplitude of the Fourier modes of a random field, while all the non-Gaussian information is in the phases).

Consider a d-dimensional random field f, with mean $\langle f\rangle = 0$ and variance $\sigma_0^2 \equiv \langle f^2\rangle$. MFs are defined for the excursion set of f, namely

$$Q_\nu = \{\mathbf{\Omega} : f(\mathbf{\Omega})/\sigma_0 > \nu\}\,. \tag{4.4}$$

According to Matsubara (2003), for a weakly non-Gaussian field in d-dimension, MFs $V_k^{(d)}(\nu)$ reads

$$
\begin{aligned}
V_k^{(d)}(\nu) \quad = \quad & \frac{1}{(2\pi)^{(k+1)/2}} \frac{\omega_d}{\omega_{d-k}\omega_k} \left(\frac{\sigma_1}{\sqrt{d}\sigma_0}\right)^k e^{-\nu^2/2} \{H_{k-1}(\nu) \\
& + \left[\frac{1}{6} S^{(0)} H_{k+2}(\nu) + \frac{k}{3} S^{(1)} H_k(\nu) + \frac{k(k-1)}{6} S^{(2)} H_{k-2}(\nu)\right] \sigma_0 + \mathcal{O}(\sigma_0^2)\right\},
\end{aligned} \tag{4.5}
$$

written in terms of Hermite polynomials $H_n(\nu)$

$$
\begin{aligned}
H_{-1}(\nu) &= \sqrt{\frac{\pi}{2}} e^{\nu^2/2} \mathrm{erfc}\left(\frac{\nu}{\sqrt{2}}\right), \\
H_0 &= 1, \\
H_1(\nu) &= \nu, \\
H_2(\nu) &= \nu^2 - 1, \\
H_3(\nu) &= \nu^3 - 3\nu, \\
H_4(\nu) &= \nu^4 - 6\nu^2 + 3,
\end{aligned} \tag{4.6}
$$

of the volume of the k-dimensional unitary sphere $\omega_k \equiv \pi^{k/2}/\Gamma(k/2+1)$, giving $\omega_0 = 1$, $\omega_1 = 2$ and $\omega_2 = \pi$ in two dimensions, and the *skewness parameters* $S^{(i)}$ defined by

$$S^{(0)} \equiv \frac{\langle f^3 \rangle}{\sigma_0^4}, \tag{4.7}$$

$$S^{(1)} \equiv -\frac{3}{4} \frac{\langle f^2 (\nabla^2 f) \rangle}{\sigma_0^2 \sigma_1^2}, \tag{4.8}$$

$$S^{(2)} \equiv -\frac{3d}{2(d-1)} \frac{\langle (\nabla f) \cdot (\nabla f)(\nabla^2 f) \rangle}{\sigma_1^4}, \tag{4.9}$$

which characterize the skewness of fluctuating fields and their derivatives. For a Gaussian field, the skewness parameters are all zero and in equation (4.5) the second line is vanishing as well.

The first line represent the case of a Gaussian field and the second one introduce a first-order deviation from Gaussianity, as reported in Hikage, Komatsu, and Matsubara (2006) for the CMB analysis. IM at 21 cm is non-Gaussian at low redshift, but it is possible to understand at which redshift it has been Gaussian looking at the appropriate frequency: SKA will give access to a redshift of $z = 27$ at the beginning of the reionization epoch.

This thesis aim to study and compare the intensity maps obtained in Chapter 3 and so it focus on the $d = 2$ case, giving $k = 0, 1, 2$. The quantity σ_j is given by

$$\sigma_j^2 \equiv \frac{1}{4\pi} \sum_l (2l+1) \left[l(l+1)\right]^j C_l W_l^2, \tag{4.10}$$

where W is a window function and quantify the effect of the experimental beam transfer function, the pixelization window function, and the extra Gaussian smoothing. The angular power spectrum in two-dimensions is defined as usual as

$$\langle a_{lm} a^*_{l'm'} \rangle = C_l \delta_{ll'} \delta_{mm'}, \tag{4.11}$$

where the harmonic coefficients a_{lm} define the usual spherical harmonic expansion of the field f in the direction $\Omega = (\vartheta, \phi)$, i.e.

$$f(\mathbf{\Omega}) = \sum_{lm} a_{lm} Y_{lm}(\mathbf{\Omega}). \tag{4.12}$$

For intensity mapping, the random field f is the standardized temperature fluctuations $f(z) = f_0/(1+z)$.

The skewness parameters (4.7), (4.8) and (4.9) can be expanded into spherical harmonics and written in terms of the angular bispectrum $B^{m_1 m_2 m_3}_{l_1 l_2 l_3} \equiv \langle a_{l_1 m_1} a_{l_2 m_2} a_{l_3 m_3} \rangle$. The final expression is Matsubara (2003)

$$\begin{aligned}
S^{(0)} &= \frac{1}{4\pi\sigma_0^4} \sum_{l_i m_i} B^{m_1 m_2 m_3}_{l_1 l_2 l_3} \mathcal{G}^{m_1 m_2 m_3}_{l_1 l_2 l_3} W_{l_1} W_{l_2} W_{l_3}, && (4.13)\\
S^{(1)} &= \frac{3}{16\pi\sigma_0^2\sigma_1^2} \sum_{l_i m_i} \frac{l_1(l_1+1) + l_2(l_2+1) + l_3(l_3+1)}{3} \\
&\quad \times B^{m_1 m_2 m_3}_{l_1 l_2 l_3} \mathcal{G}^{m_1 m_2 m_3}_{l_1 l_2 l_3} W_{l_1} W_{l_2} W_{l_3}, && (4.14)\\
S^{(2)} &= \frac{3}{8\pi\sigma_1^4} \sum_{l_i m_i} \left\{ \frac{\left[l_1(l_1+1) + l_2(l_2+1) - l_3(l_3+1)\right] l_3(l_3+1) + (\text{cyc.})}{3} \right\} \\
&\quad \times B^{m_1 m_2 m_3}_{l_1 l_2 l_3} \mathcal{G}^{m_1 m_2 m_3}_{l_1 l_2 l_3} W_{l_1} W_{l_2} W_{l_3}, && (4.15)
\end{aligned}$$

where (cyc.) means the addition of terms with the same cyclic order of the subscripts as the previous term and $\mathcal{G}^{m_1 m_2 m_3}_{l_1 l_2 l_3}$ is the Gaunt integral

$$\mathcal{G}^{m_1 m_2 m_3}_{l_1 l_2 l_3} \equiv \int d\hat{\mathbf{n}} Y_{l_1 m_1}(\hat{\mathbf{n}}) Y_{l_2 m_2}(\hat{\mathbf{n}}) Y_{l_3 m_3}(\hat{\mathbf{n}}). \tag{4.16}$$

The summation over m_i can be done by using

$$B^{m_1 m_2 m_3}_{l_1 l_2 l_3} = \mathcal{G}^{m_1 m_2 m_3}_{l_1 l_2 l_3} b_{l_1 l_2 l_3}. \tag{4.17}$$

where $b_{l_1 l_2 l_3}$ is the *reduced bispectrum.* The power spectrum is

$$C_l = \frac{2}{\pi} \int_0^\infty k^2 dk P(k) g^2_{Tl}(k), \tag{4.18}$$

with $g_{Tl}(k)$ is the normalized Bessel transform of the selection function $S(r)$ (Mo, van den Bosch, and White, 2010)

$$g_{Tl}(k) = \frac{\int S(r) j_l(kr) r^2 \mathrm{d}r}{\int S(r) r^2 \mathrm{d}r}. \tag{4.19}$$

Approximating $S(r)$ by a Dirac delta function $\delta^{(D)}(r - d^*)$, where d^* is the comoving distance of IM (the slice selected in Chapter 3). Then equation (4.18) becomes

$$C_l = \frac{2}{\pi} \int_0^\infty k^2 P(k) j_l(kd^*)^2 \mathrm{d}k. \tag{4.20}$$

Using the power spectrum computed from the dark matter halo catalogues, it is possible to compute C_l and therefore the express analytically the MFs. It is important to stress that this third-order model is not sufficient to describe the highly non-Gaussian field observed in 21 cm IM. However, one can fairly expect that it is well-suited for IM at sufficiently low frequency, i.e. probing very high redshifts. The Fig. 4.2 illustrate the

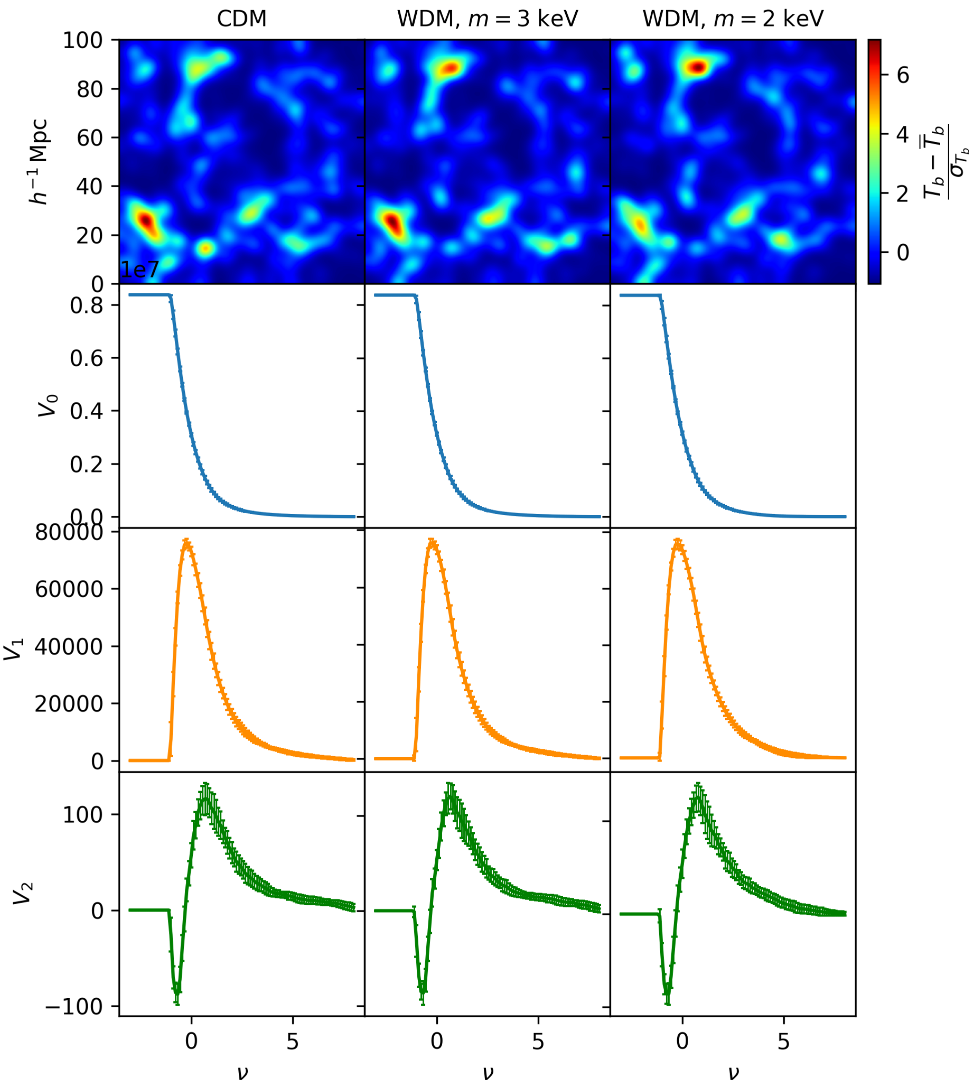

Figure 4.2: Intensity maps and MFs for $z = 1$.

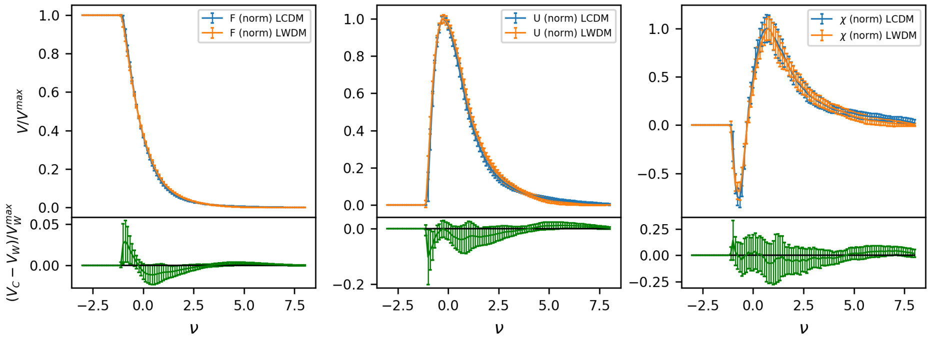

Figure 4.3: Referring to Fig. 4.2, MFs comparison for ΛCDM and ΛWDM with $m = 2$ keV, at $z = 1$.

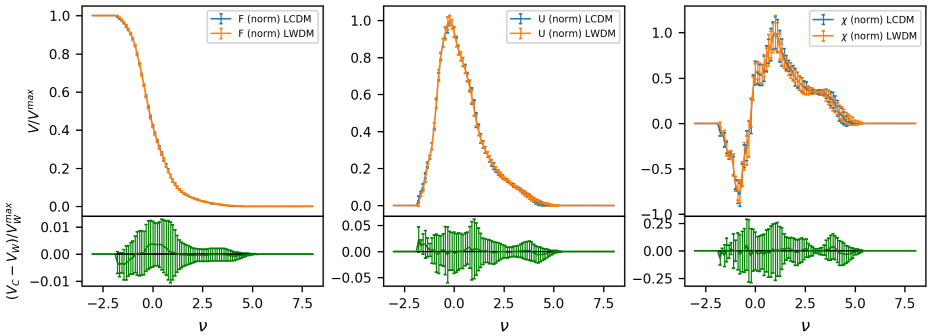

Figure 4.4: Referring to Fig. 4.12, MFs comparison for ΛCDM and ΛWDM with $m = 2$ keV, at $z = 3$.

highly non-Gaussian temperature field simulated at $z = 1$ for the three cosmologies along with the corresponding MFs of the standardized temperature as function of the threshold ν. Increasing from negative to positive values, only the high-temperature regions contribute to the surface V_0, which therefore decreases. V_1 and V_2 have a less trivial dependence, only qualitatively resembling the curves expected for a Gaussian field. The negative values of V_2 corresponds to temperature underdensities, which trace the cosmic voids, while positive peaks (especially visibles in maps at $z \geq 3$; see Appendix) corresponds to excess of temperatures, which trace the haloes with higher mass up to about $10^{12} M_{\odot}$.

4.2 Analysis

Minkowski functionals have been computed for the intensity maps obtained in Chapter 3 using `minkfncts2d` libraries (Mantz, Jacobs, and Mecke, 2008). For every redshift and every cosmology, 50 Monte Carlo simulations of a single slice have been computed. The mean and the standard deviation of the MFs have been calculated and the results

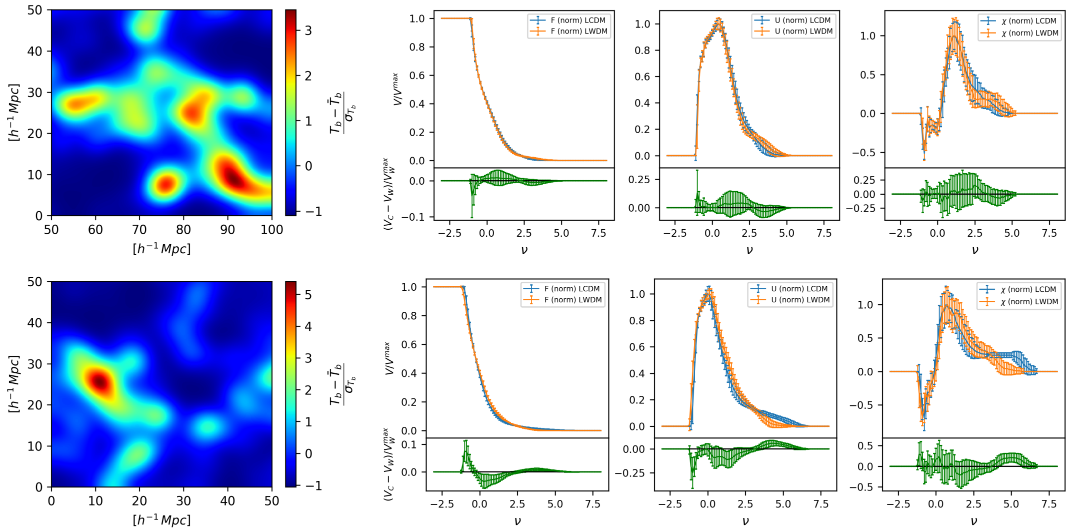

Figure 4.5: Intensity maps and MFs for $z = 1$ for a smaller regions.

are shown in Figure 4.2 for $z = 1$. For the two redshifts, in Figures 4.3 ($z = 1$) and 4.4 ($z = 3$), the comparison between the ΛCDM and ΛWDM with $m = 2$ keV cosmologies are reported. We decided not to show the ΛWDM with $m = 3$ keV cosmology since the differences with the two other models are not visible. Even though the error bars of the differences between the cosmologies calculated by quadratic propagation (bottom panels in Figure 4.3 and 4.4) are always compatible with zero, e.g. MFs can not identify the different cosmologies, there is room for interesting remarks. First, in Figures 4.4 and the analogues figures in Appendix there is a trend for V_0 at low threshold: the difference between the ΛCDM and the ΛWDM has a negative minimum and immediately after a positive maximum. The minimum can be interpreted as a signature of voids, which in ΛWDM are typically larger than in ΛCDM due to the larger free-streaming length of WDM compared to CDM (rigorously infinite). In Appendix the results of the same analysis for redshifts $z = 2$, 4, 5 and for all the slices analyzed are reported.

Consider the Figure 4.3, the differences between the two DM models is more evident than for other redshifts and slices, especially for the Euler characteristic. Looking at the corresponding intensity maps, the differences are remarkable near the denser regions (left-bottom quarter of the figure). Consequently, one can think about measuring MFs only in regions where the emission temperature is way above the mean value. An interesting example is reported in Figure 4.5, where only a portion of the original maps have been analyzed, showing a more evident discrepancy for ΛCDM and ΛWDM ($m = 2$ keV) cosmologies. A systematic algorithm to select the appropriate regions has not been defined yet and not all the maps present the same property. It will be matter of further studies.

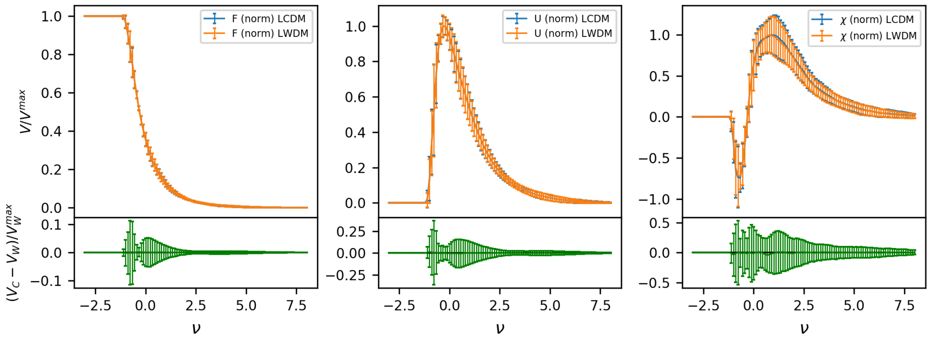

Figure 4.6: MFs for $z = 1$ considering all the slices analyzed.

Finally, all the MFs computed for a given redshift have been weighted and the results are shown in Figure 4.6 (in Appendix the analogues figures for redshifts $z = 2, 3, 4, 5$). Since the slices are not adjacent, their correlation is reduced; averaging all of them provides a first rough estimate of the MFs for larger surveys. The perfect agreement between the two cosmologies suggests even more the necessity to investigate the small scales structure to get a better insight into the dark matter sector.

Interestingly enough, while for redshift $z < 2$ the Euler characteristic V_2 is smoothing decreasing with threshold, at higher redshift small but robust wiggles not confused with noise appear for positive large values of the threshold ($2 < \nu < 5$). They suggest a spongy-like topology of the temperature field in the high-density regions, i.e. holes appear within the largest peaks of temperature. This is a signature of a non-trivial reionization process, which seems however independent of the nature of dark matter: at these values of threshold, the relative difference between CDM and WDM intensity maps are always consistent with zero.

Conclusion and future perspectives

During this thesis several statistical tools have been explored and developed. Firstly, Monte Carlo simulations have been implemented using a standard parametric method and a new non-parametric method that better grasps the physical processes occurring during the reionization as described by hydrodynamical simulations, allowing us to obtain neutral hydrogen catalogues from both cold and warm dark matter haloes catalogues. Then an algorithm to create two-dimensional intensity maps has been realized flexible enough to be applied to large cosmological volumes and to every emission line and dedicated survey, accounting for the specific spectral response function and angular resolution. Indeed this algorithm can be used both for cosmological and astrophysical studies. The morphology of matter or gas distribution is completely described using Minkowski functionals, which are able to provide information and constraints on different cosmologies.

Intensity mapping applied to 21 cm emission line is a very promising research field. A large number of radio-telescopes are devoted to survey large portions of the sky as LOFAR (van Haarlem et al., 2013) and SKA-1 (Square Kilometre Array Cosmology Science Working Group et al., 2018). The preliminary simulations work seems to be able to provide strong information and constraint on cosmology and astrophysics, spacing from primordial non-Gaussianity to dark matter particles and models.

Several improvements of this work are possible. The HI halo mass, that we used to simulate HI haloes starting from dark matter catalogues, is not completely known so far (Spinelli et al., 2019): as reported in Chapter 2, at large redshift the function does not reproduce the correct amount of HI (measured using several astrophysical bounds) and its evolution is not totally understood yet. The resolution of the simulations could be also improved using a finer grid with cell size comparable to the virialization radius of an HI halo: the next step would be based on simulations at higher resolution, requiring a much larger computational power and resources. This operation would upgrade the quality of the maps. The rms-variance of the Gaussian smoothing depends on $(1 + z)/D$ (Bull et al., 2015) where D is the diameter of the single dish and its value becomes comparable to the size of the intensity map we used. Therefore, considering catalogues with a larger box-size would improve the resolution of the maps and the analysis consequently.

This thesis has not addressed one major problem of the data analysis, i.e. the contamination of the signal by foregrounds (Cunnington et al., 2019). Regardless the cleaning technique (Villaescusa-Navarro, Alonso, and Viel, 2017), some residual foreground might still contaminate the final maps; a complete analysis of MFs should account for this occurrence by including in the final maps a controlled fraction of foregrounds. Their impact as function of the threshold level is not trivial and could be degenerate with a potential, genuine signature of the WDM. The problem of modeling the galactic and extra-galactic foregrounds is an open research field in intensity mapping studies, which so far produced several models and cleaning techniques. The cross-correlations with other emission lines, such as [CII] or [OIII], and with galaxy surveys (Padmanabhan, Refregier, and Amara, 2019) such as Euclid (Laureijs et al., 2011) would be decisive to study the reionization epoch and the HI evolution.

Appendix

The MFs comparison for different slices at redshifts $z = 1$ and $z = 3$ are shown in Figures 4.7 and 4.13. The complete results presented in Chapter 4 are here shown for redshifts $z = 2$ (Figures 4.8, 4.9, 4.10 and 4.11), $z = 3$ (Figures 4.12, 4.13 and 4.14) $z = 4$ (Figures 4.15, 4.16, 4.17 and 4.18) and $z = 5$ (Figures 4.19, 4.20, 4.21 and 4.22).

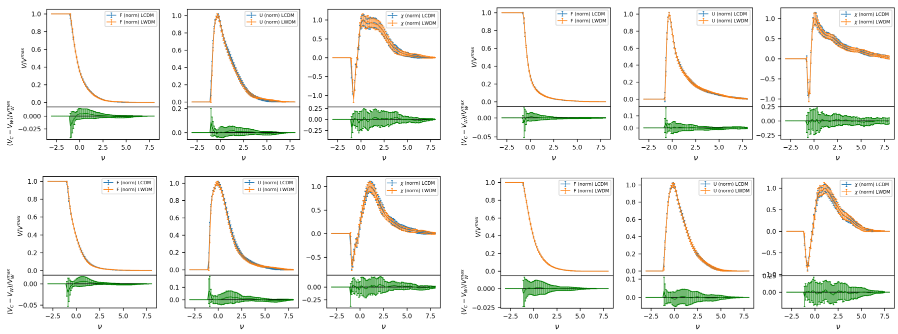

Figure 4.7: MFs comparison for ΛCDM and ΛWDM with $m = 2$ keV, at $z = 1$, for different slices.

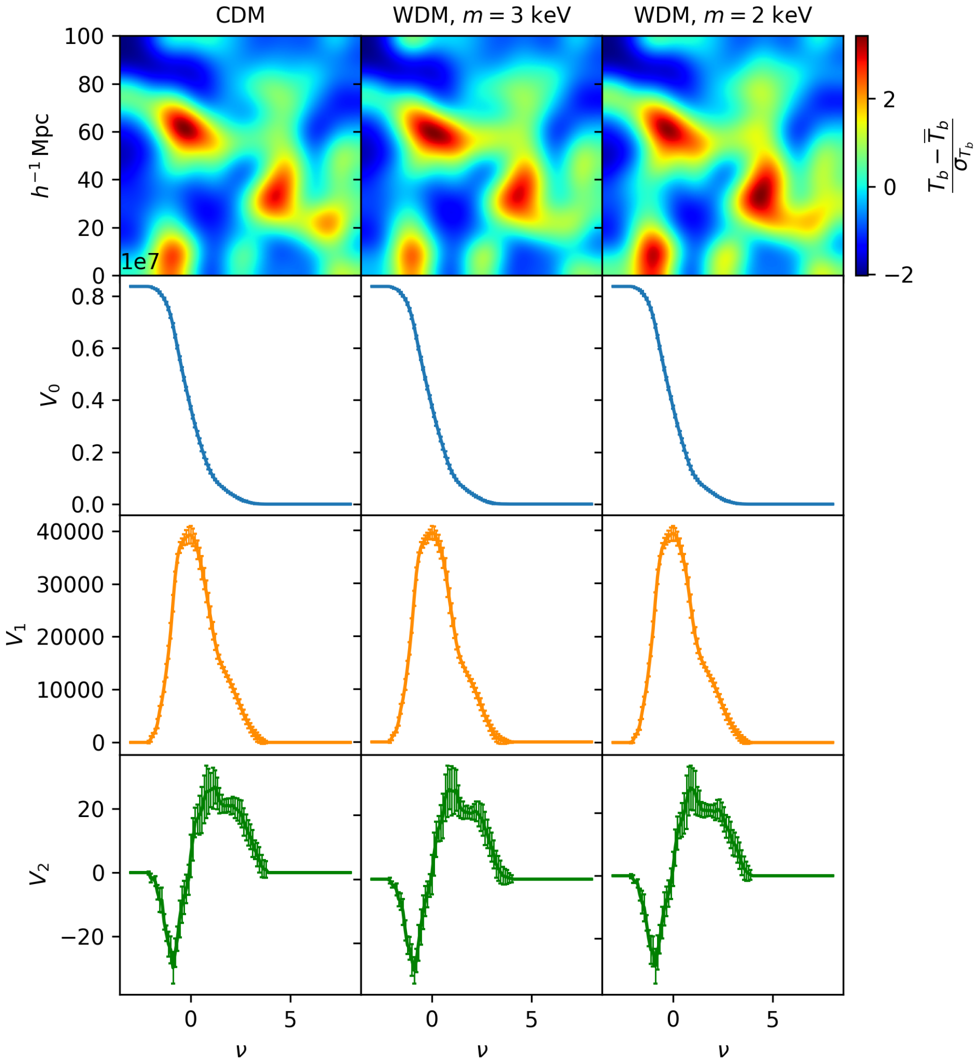

Figure 4.8: Intensity maps and MFs for $z = 2$.

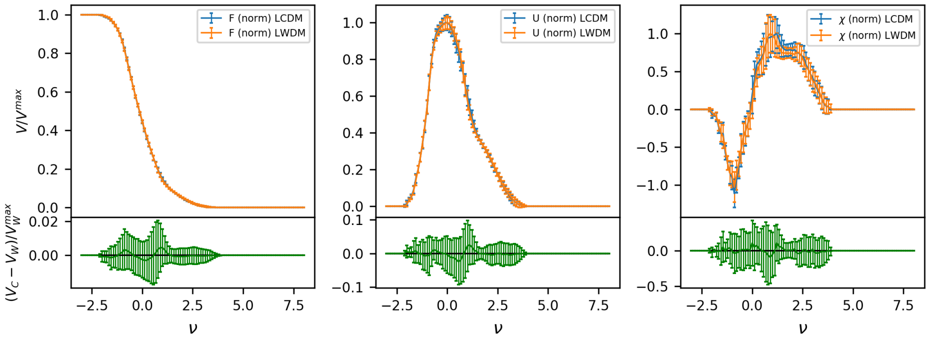

Figure 4.9: Referring to Fig. 4.8, MFs comparison for ΛCDM and ΛWDM with $m = 2$ keV, at $z = 2$.

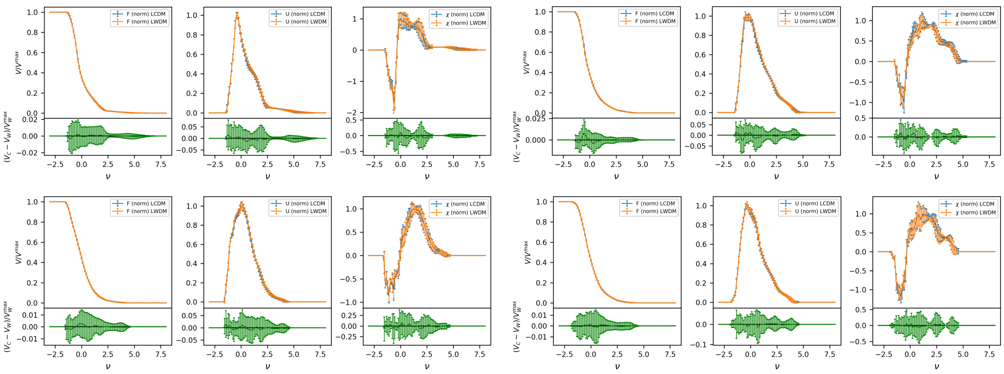

Figure 4.10: MFs comparison for ΛCDM and ΛWDM with $m = 2$ keV, at $z = 2$, for different slices.

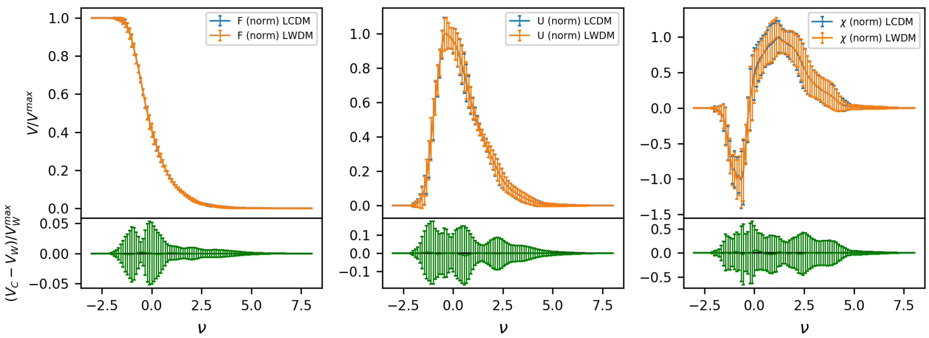

Figure 4.11: MFs for $z = 2$ considering all the slices analyzed.

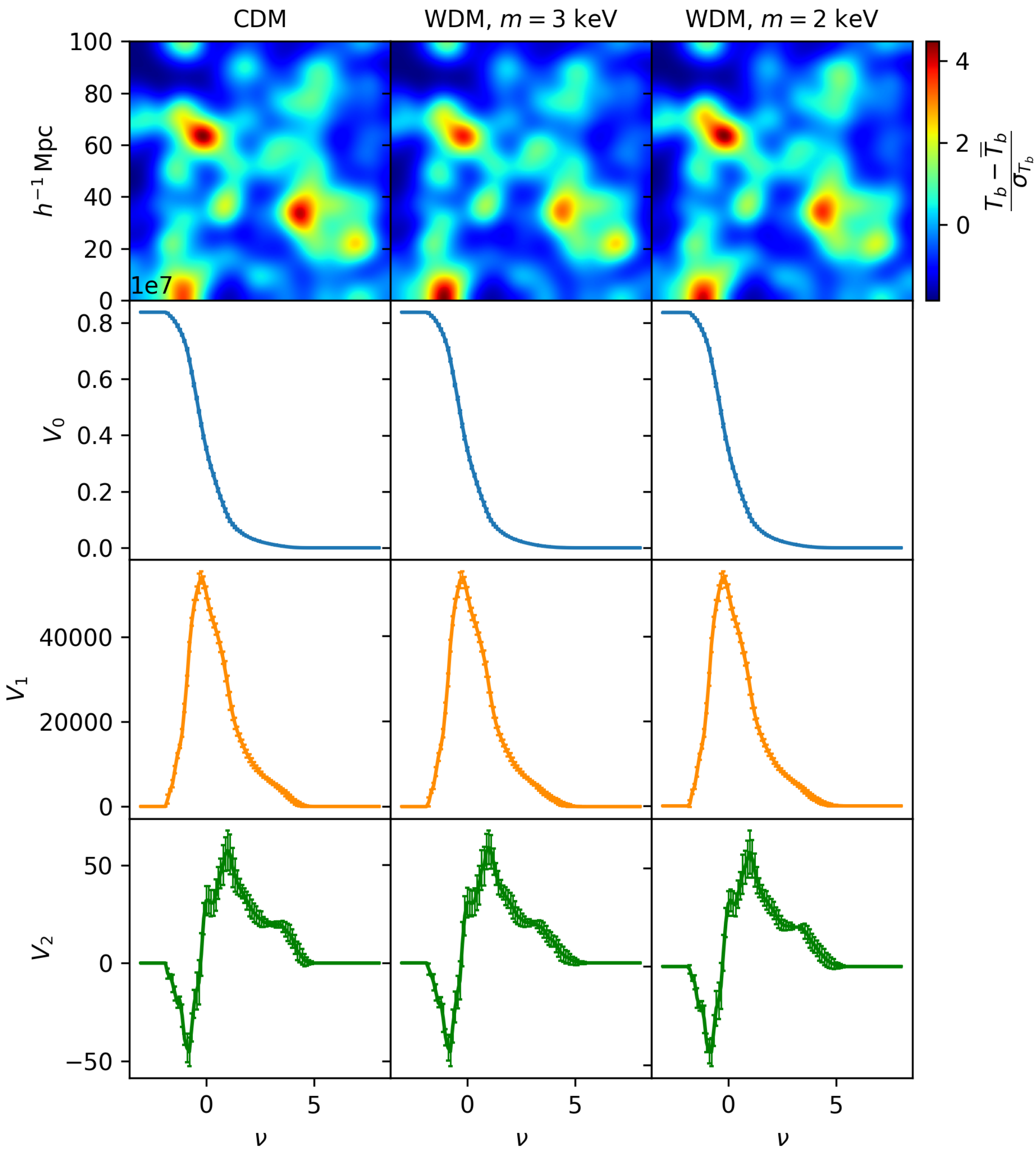

Figure 4.12: Intensity maps and MFs for $z = 3$.

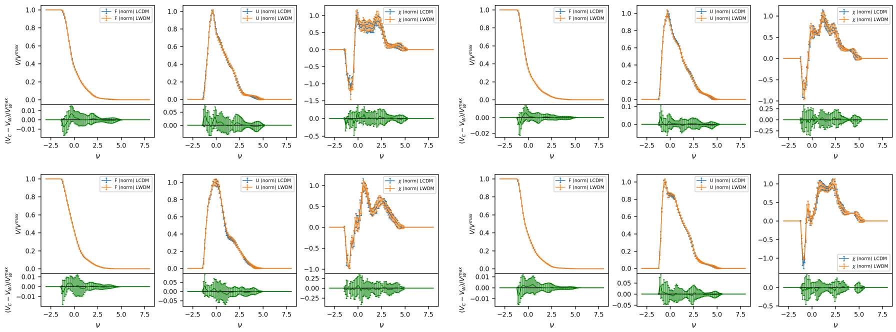

Figure 4.13: MFs comparison for ΛCDM and ΛWDM with $m = 2$ keV, at $z = 3$, for different slices.

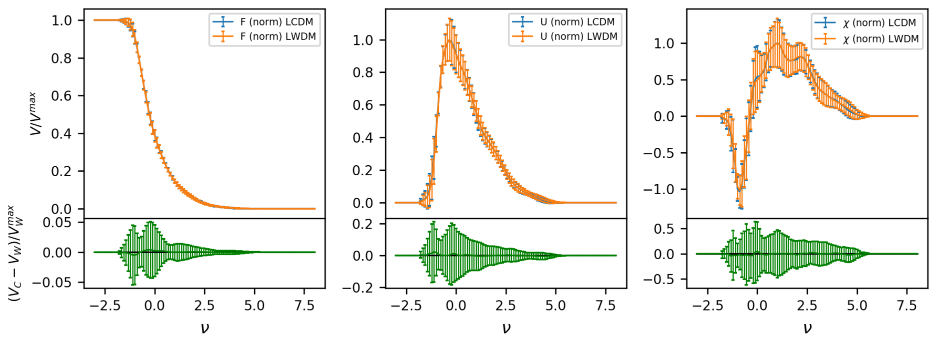

Figure 4.14: MFs for $z = 3$ considering all the slices analyzed.

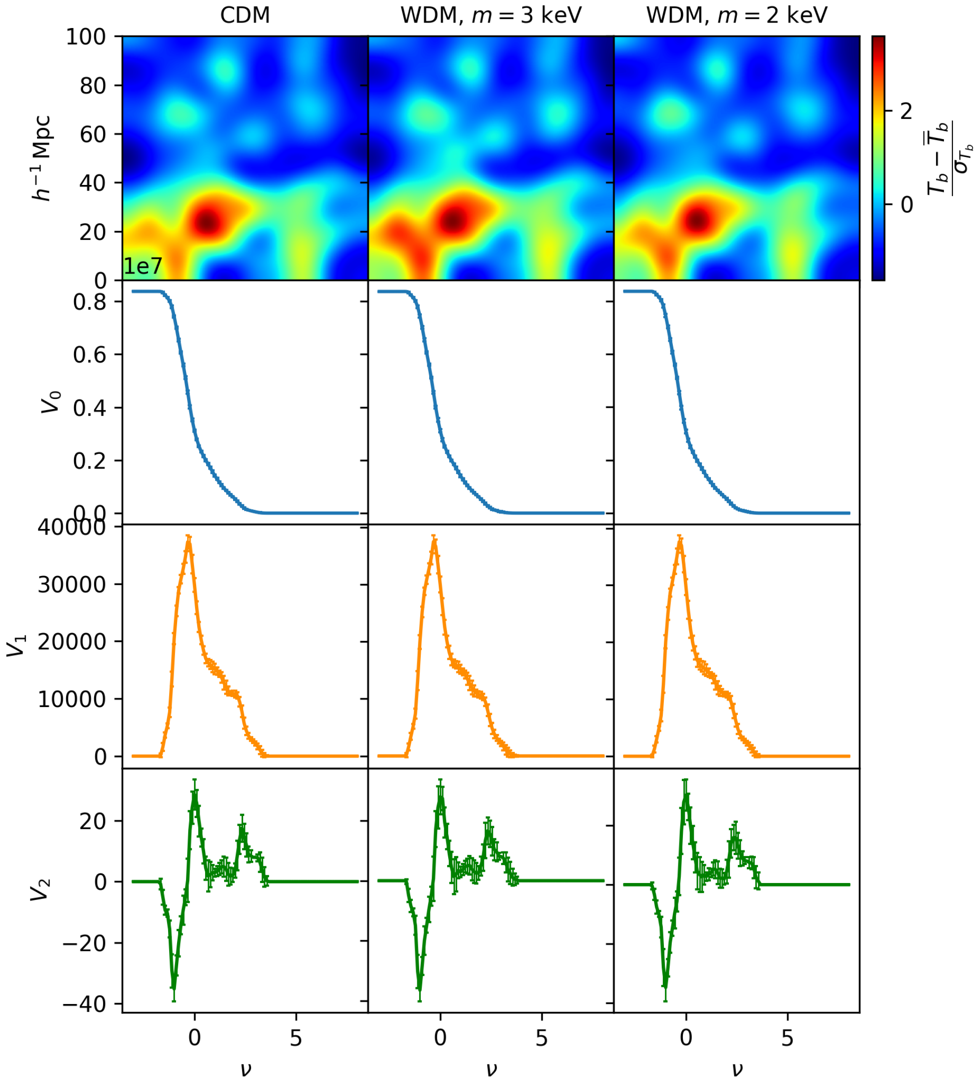

Figure 4.15: Intensity maps and MFs for $z = 4$.

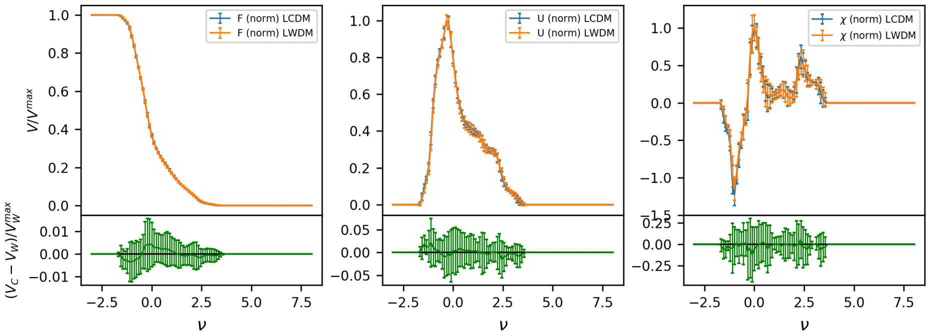

Figure 4.16: Referring to Fig. 4.15, MFs comparison for ΛCDM and ΛWDM with $m = 2$ keV, at $z = 4$.

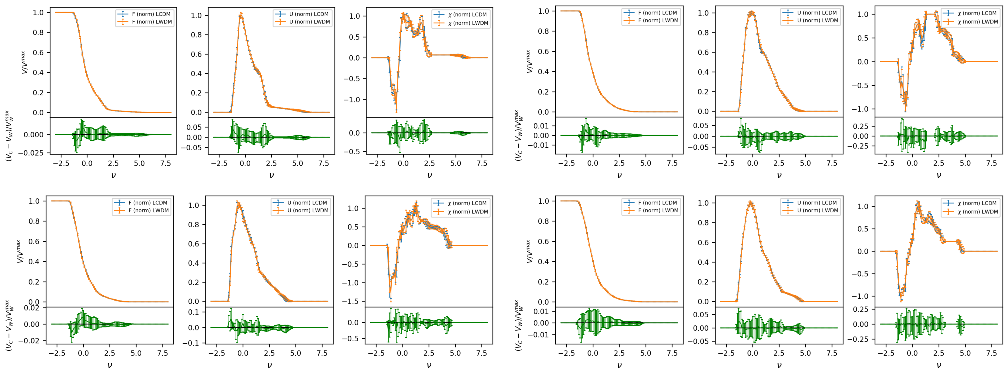

Figure 4.17: MFs comparison for ΛCDM and ΛWDM with $m = 2$ keV, at $z = 4$, for different slices.

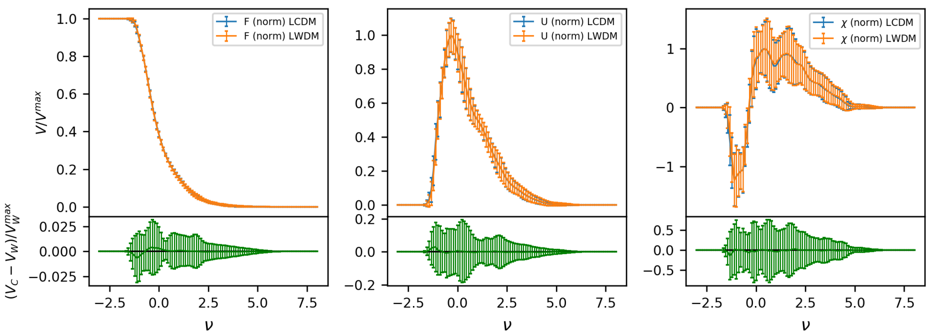

Figure 4.18: MFs for $z = 4$ considering all the slices analyzed.

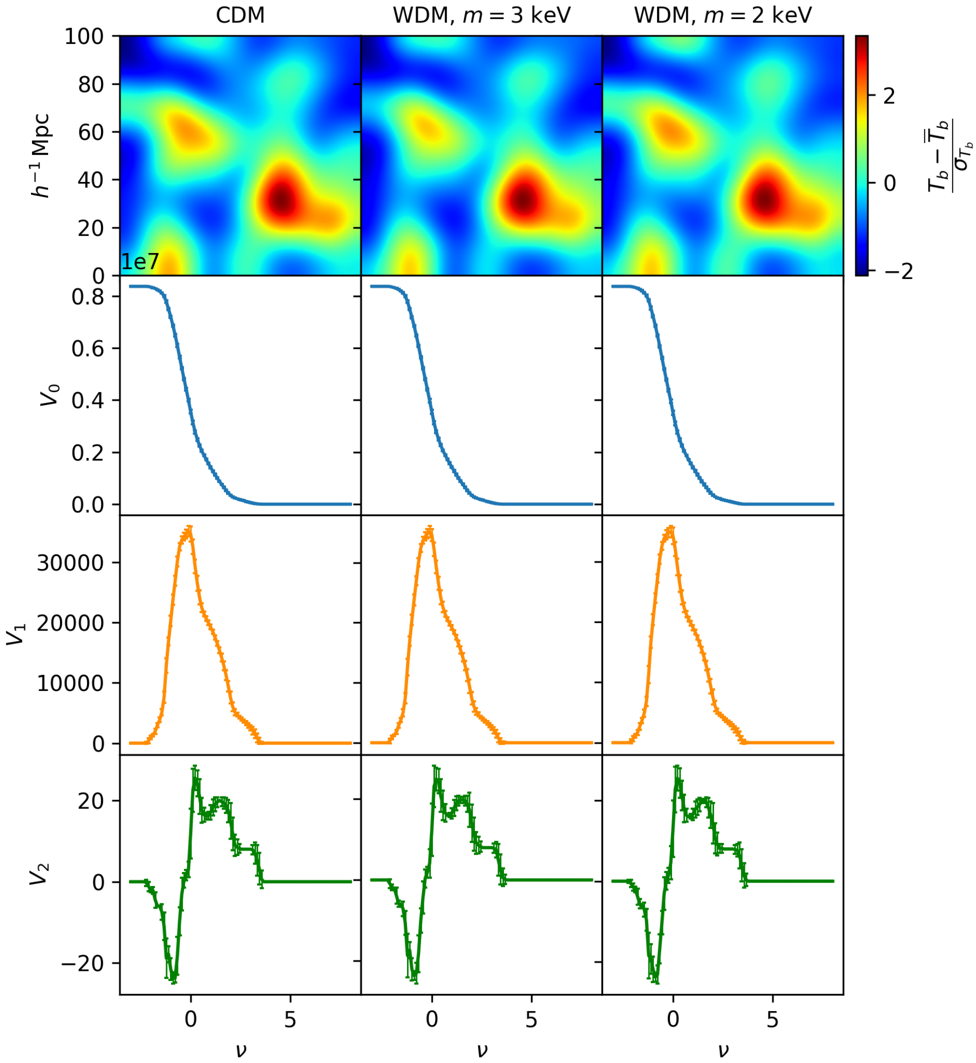

Figure 4.19: Intensity maps and MFs for $z = 5$.

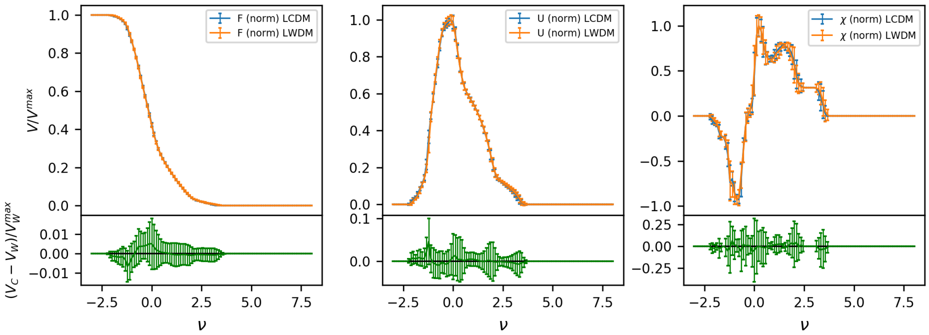

Figure 4.20: Referring to Fig. 4.19, MFs comparison for ΛCDM and ΛWDM with $m = 2$ keV, at $z = 5$.

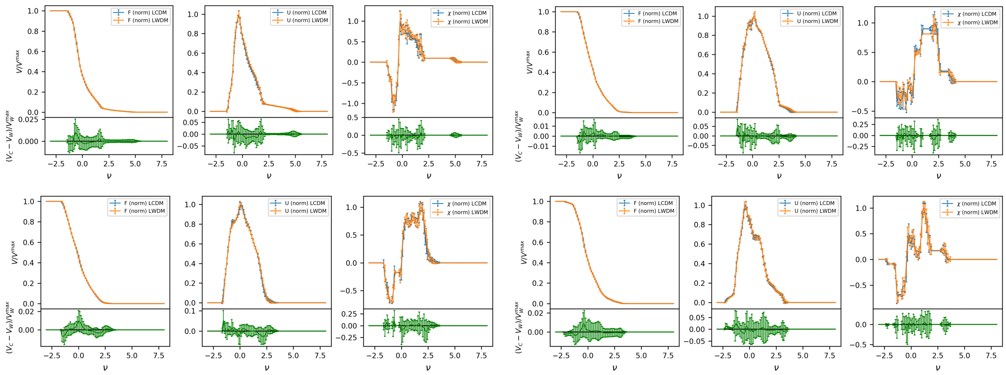

Figure 4.21: MFs comparison for ΛCDM and ΛWDM with $m = 2$ keV, at $z = 5$, for different slices.

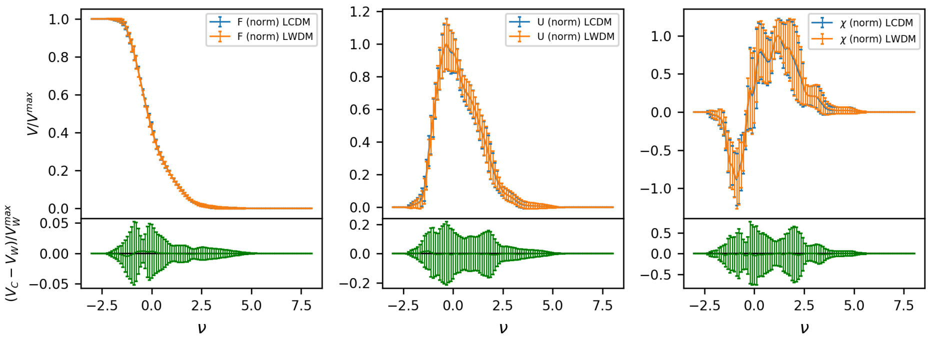

Figure 4.22: MFs for $z = 5$ considering all the slices analyzed.

Bibliography

Anderson, C. J. et al. (May 2018). "Low-amplitude clustering in low-redshift 21-cm intensity maps cross-correlated with 2dF galaxy densities". In: *MNRAS* 476(3), pp. 3382–3392. arXiv: 1710.00424 [astro-ph.CO].

Aprile, E. et al. (Apr. 2019). "Constraining the Spin-Dependent WIMP-Nucleon Cross Sections with XENON1T". In: *Physical Review Letters* 122(14), 141301, p. 141301. arXiv: 1902.03234 [astro-ph.CO].

Aubert, Dominique, Nicolas Deparis, and Pierre Ocvirk (Nov. 2015). "EMMA: an adaptive mesh refinement cosmological simulation code with radiative transfer". In: *MNRAS* 454(1), pp. 1012–1037. arXiv: 1508.07888 [astro-ph.IM].

Bagla, J. S., Nishikanta Khandai, and Kanan K. Datta (Sept. 2010). "HI as a probe of the large-scale structure in the post-reionization universe". In: *MNRAS* 407(1), pp. 567–580. arXiv: 0908.3796 [astro-ph.CO].

Barkana and Loeb (July 2001). "In the beginning: the first sources of light and the reionization of the universe". In: *Physics Reports* 349(2), pp. 125–238. arXiv: astro-ph/0010468 [astro-ph].

Baugh, C. M. et al. (Mar. 2019). "Galaxy formation in the Planck Millennium: the atomic hydrogen content of dark matter halos". In: *MNRAS* 483(4), pp. 4922–4937. arXiv: 1808.08276 [astro-ph.GA].

Bode, Paul, Jeremiah P. Ostriker, and Neil Turok (July 2001). "Halo Formation in Warm Dark Matter Models". In: *Astrophysics Journal* 556(1), pp. 93–107. arXiv: astro-ph/0010389 [astro-ph].

Bull, Philip et al. (Apr. 2015). "Late-time Cosmology with 21 cm Intensity Mapping Experiments". In: *Astrophysics Journal* 803(1), 21. arXiv: 1405.1452 [astro-ph.CO].

Cantalupo, Sebastiano et al. (Feb. 2014). "A cosmic web filament revealed in Lyman-α emission around a luminous high-redshift quasar". In: *Nature* 506(7486), pp. 63–66. arXiv: 1401.4469 [astro-ph.CO].

Carucci, Isabella P. et al. (July 2015). "Warm dark matter signatures on the 21cm power spectrum: intensity mapping forecasts for SKA". In: *Journal of Cosmology and Astroparticle Physics* 2015(7), 047, p. 047. arXiv: 1502.06961 [astro-ph.CO].

Chung, Daniel J. H., Edward W. Kolb, and Antonio Riotto (Jan. 1999). "Superheavy dark matter". In: *Particle Review D* 59(2), 023501, p. 023501. arXiv: hep-ph/9802238 [hep-ph].

Ciardi, Stoehr, and White (Aug. 2003). “Simulating intergalactic medium reionization”. In: *MNRAS* 343(4), pp. 1101–1109. arXiv: astro-ph/0301293 [astro-ph].

Cowsik, R. and J. McClelland (Sept. 1972). “An Upper Limit on the Neutrino Rest Mass”. In: *Physics Review Letters* 29(10), pp. 669–670.

Cui, Weiguang et al. (Nov. 2008). “An Ideal Mass Assignment Scheme for Measuring the Power Spectrum with Fast Fourier Transforms”. In: *Astrophysics Journal* 687(2), pp. 738–744. arXiv: 0804.0070 [astro-ph].

Cunnington, Steven et al. (Oct. 2019). “Impact of foregrounds on H I intensity mapping cross-correlations with optical surveys”. In: *MNRAS* 488(4), pp. 5452–5472. arXiv: 1904.01479 [astro-ph.CO].

Despali, Giulia et al. (Mar. 2016). “The universality of the virial halo mass function and models for non-universality of other halo definitions”. In: *MNRAS* 456(3), pp. 2486–2504. arXiv: 1507.05627 [astro-ph.CO].

Ewen, H. I. and E. M. Purcell (Sept. 1951). “Observation of a Line in the Galactic Radio Spectrum: Radiation from Galactic Hydrogen at 1,420 Mc./sec.” In: *Nature* 168(4270), p. 356.

Field, George B. (Jan. 1958). “Excitation of the Hydrogen 21-CM Line”. In: *Proceedings of the IRE* 46, pp. 240–250.

Gong, Yan et al. (Jan. 2012). “Intensity Mapping of the [C II] Fine Structure Line during the Epoch of Reionization”. In: *The Astrophysical Journal* 745(1), 49, p. 49. arXiv: 1107.3553 [astro-ph.CO].

Gott J. Richard, III, Adrian L. Melott, and Mark Dickinson (July 1986). “The Sponge-like Topology of Large-Scale Structure in the Universe”. In: *Astrophysics Journal* 306, p. 341.

Hadwiger, Hugo (1957). “Vorlesungen über Inhalt, Oberfläche und Isoperimetrie”. In:

Hand, Nick et al. (Apr. 2019). *nbodykit: Massively parallel, large-scale structure toolkit.* ascl: 1904.027.

Henry, J. Patrick (May 2000). “Measuring Cosmological Parameters from the Evolution of Cluster X-Ray Temperatures”. In: *The Astrophysical Journal* 534(2), pp. 565–580. arXiv: astro-ph/0002365 [astro-ph].

Hikage, Chiaki, Eiichiro Komatsu, and Takahiko Matsubara (Dec. 2006). “Primordial Non-Gaussianity and Analytical Formula for Minkowski Functionals of the Cosmic Microwave Background and Large-Scale Structure”. In: *Astrophysics Journal* 653(1), pp. 11–26. arXiv: astro-ph/0607284 [astro-ph].

Hu, Wenkai et al. (Oct. 2019). “An accurate low-redshift measurement of the cosmic neutral hydrogen density”. In: *MNRAS* 489(2), pp. 1619–1632. arXiv: 1907.10375 [astro-ph.GA].

Jansky, K. G. (1982). “1933, Electrical Disturbances Apparently of Extraterrestrial Origin”. In: *Classics in Radio Astronomy, Studies in the History of Modern Science. Volume 10. Edited by W.T. Sullivan, III. Dordrecht, D. Reidel Publishing Co, 1982, p.23.* Vol. 10, p. 23.

Jedamzik, Karsten (July 1995). “The Cloud-in-Cloud Problem in the Press-Schechter Formalism of Hierarchical Structure Formation”. In: *Astrphysics Journal* 448, p. 1. arXiv: astro-ph/9408080 [astro-ph].

Kolb, Edward W. and Michael S. Turner (1990). *The early universe*. Vol. 69.

Kovetz, Ely D. et al. (Sept. 2017). “Line-Intensity Mapping: 2017 Status Report”. In: arXiv: 1709.09066 [astro-ph.CO].

Lagos, C. D. P. et al. (May 2014). “Which galaxies dominate the neutral gas content of the Universe?” In: *MNRAS* 440(1), pp. 920–941. arXiv: 1310.4178 [astro-ph.CO].

Laureijs, R. et al. (Oct. 2011). “Euclid Definition Study Report”. In: *arXiv e-prints*, arXiv:1110.3193, arXiv:1110.3193. arXiv: 1110.3193 [astro-ph.CO].

Lewis, Antony and Anthony Challinor (Feb. 2011). *CAMB: Code for Anisotropies in the Microwave Background*. ascl: 1102.026.

Mantz, Jacobs, and Mecke (Dec. 2008). “Utilizing Minkowski functionals for image analysis: a marching square algorithm”. In: *Journal of Statistical Mechanics: Theory and Experiment* 2008(12), p. 12015.

Matsubara, Takahiko (Feb. 2003). “Statistics of Smoothed Cosmic Fields in Perturbation Theory. I. Formulation and Useful Formulae in Second-Order Perturbation Theory”. In: *Astrophysics Journal* 584(1), pp. 1–33.

Mecke, Buchert, and H. Wagner (Aug. 1994). “Robust morphological measures for large-scale structure in the Universe”. In: *Astronomy and Astrophysics* 288, pp. 697–704. arXiv: astro-ph/9312028 [astro-ph].

Mo, van den Bosch, and White (May 2010). *Galaxy Formation and Evolution*.

Naoz, S. and R. Barkana (May 2007). “The formation and gas content of high-redshift galaxies and minihaloes”. In: *MNRAS* 377(2), pp. 667–676. arXiv: astro-ph/0612004 [astro-ph].

Padmanabhan, Hamsa, Alexandre Refregier, and Adam Amara (Sept. 2019). “Cross-correlating 21 cm and galaxy surveys: implications for cosmology and astrophysics”. In: *arXiv e-prints*. arXiv: 1909.11104 [astro-ph.CO].

Pawlik, Andreas H., Joop Schaye, and Claudio Dalla Vecchia (Aug. 2015). “Spatially adaptive radiation-hydrodynamical simulations of galaxy formation during cosmological reionization”. In: *MNRAS* 451(2). arXiv: 1501.01980 [astro-ph.CO].

Peter, Patrick and Jean-Philippe Uzan (2009). *Primordial cosmology*. Oxford Graduate Texts. Oxford Univ. Press: Oxford. URL: https://cds.cern.ch/record/1208401.

Planck Collaboration (Sept. 2016). “Planck 2015 results. XIII. Cosmological parameters”. In: *Astronomy and Astrophysical Journal* 594, A13, A13. arXiv: 1502.01589 [astro-ph.CO].

Planck Collaboration et al. (July 2018). “Planck 2018 results. VI. Cosmological parameters”. In: *arXiv e-prints*, arXiv:1807.06209, arXiv:1807.06209. arXiv: 1807.06209 [astro-ph.CO].

Press, William H. and Paul Schechter (Feb. 1974). “Formation of Galaxies and Clusters of Galaxies by Self-Similar Gravitational Condensation”. In: *The Astrophysics Journal* 187, pp. 425–438.

Pritchard, Jonathan R. and Steven R. Furlanetto (Apr. 2006). "Descending from on high: Lyman-series cascades and spin-kinetic temperature coupling in the 21-cm line". In: *MNRAS* 367(3), pp. 1057–1066. arXiv: `astro-ph/0508381 [astro-ph]`.

Pritchard and Loeb (Aug. 2012). "21 cm cosmology in the 21st century". In: *Reports on Progress in Physics* 75(8), 086901, p. 086901. arXiv: `1109.6012 [astro-ph.CO]`.

Santos, Mário G. et al. (Dec. 2008). "Cosmic Reionization and the 21 cm Signal: Comparison between an Analytical Model and a Simulation". In: *The Astrophysical Journal* 689(1), pp. 1–16. arXiv: `0708.2424 [astro-ph]`.

Schneider, Aurel et al. (June 2012). "Non-linear evolution of cosmological structures in warm dark matter models". In: *MNRAS* 424(1), pp. 684–698. ISSN: 0035-8711. URL: `http://dx.doi.org/10.1111/j.1365-2966.2012.21252.x`.

Sheth, Mo, and Tormen (May 2001). "Ellipsoidal collapse and an improved model for the number and spatial distribution of dark matter haloes". In: *MNRAS* 323(1), pp. 1–12. arXiv: `astro-ph/9907024 [astro-ph]`.

Sheth and Tormen (Sept. 1999). "Large-scale bias and the peak background split". In: *MNRAS* 308(1), pp. 119–126. arXiv: `astro-ph/9901122 [astro-ph]`.

Spinelli, Marta et al. (Sept. 2019). "The atomic Hydrogen content of the post-reionization Universe". In: *arXiv e-prints*, arXiv:1909.02242, arXiv:1909.02242. arXiv: `1909.02242 [astro-ph.CO]`.

Springel, Volker et al. (Mar. 2018). "First results from the IllustrisTNG simulations: matter and galaxy clustering". In: *MNRAS* 475(1), pp. 676–698. arXiv: `1707.03397 [astro-ph.GA]`.

Square Kilometre Array Cosmology Science Working Group et al. (Nov. 2018). "Cosmology with Phase 1 of the Square Kilometre Array; Red Book 2018: Technical specifications and performance forecasts". In: *arXiv e-prints*. arXiv: `1811.02743 [astro-ph.CO]`.

Taylor, A. R. (Mar. 2013). "The Square Kilometre Array". In: *Neutron Stars and Pulsars: Challenges and Opportunities after 80 years*. Ed. by Joeri van Leeuwen. Vol. 291. IAU Symposium, pp. 337–341.

van Haarlem, M. P. et al. (Aug. 2013). "LOFAR: The LOw-Frequency ARray". In: *Astronomy and Astrophysics* 556, A2, A2. arXiv: `1305.3550 [astro-ph.IM]`.

Viel, Matteo et al. (Mar. 2005). "Constraining warm dark matter candidates including sterile neutrinos and light gravitinos with WMAP and the Lyman-α forest". In: *Physics Review D* 71(6), 063534, p. 063534. arXiv: `astro-ph/0501562 [astro-ph]`.

Villaescusa-Navarro, Francisco (Nov. 2018). *Pylians: Python libraries for the analysis of numerical simulations*. ascl: `1811.008`.

Villaescusa-Navarro, Francisco, David Alonso, and Matteo Viel (Apr. 2017). "Baryonic acoustic oscillations from 21 cm intensity mapping: the Square Kilometre Array case". In: *MNRAS* 466(3), pp. 2736–2751. arXiv: `1609.00019 [astro-ph.CO]`.

Villaescusa-Navarro, Francisco, Shy Genel, et al. (Oct. 2018). "Ingredients for 21 cm Intensity Mapping". In: *The Astrophysical Journal* 866(2), 135, p. 135. arXiv: `1804.09180 [astro-ph.CO]`.

Watson, William A. et al. (Aug. 2013). “The halo mass function through the cosmic ages”. In: *MNRAS* 433(2), pp. 1230–1245. arXiv: `1212.0095 [astro-ph.CO]`.
Wyithe, J. Stuart B. and Miguel F. Morales (Aug. 2007). “Biased reionization and non-Gaussianity in redshifted 21-cm intensity maps of the reionization epoch”. In: *MNRAS* 379(4), pp. 1647–1657. arXiv: `astro-ph/0703070 [astro-ph]`.